QUARTERLY JOURNAL
OF THE
ROYAL METEOROLOGICAL SOCIETY

Vol. 127 OCTOBER 2001 Part A No. 577

Q. J. R. Meteorol. Soc. (2001), **127**, pp. 2209–2245

Wavelet analysis and the governing dynamics of a large-amplitude mesoscale gravity-wave event along the East Coast of the United States

By FUQING ZHANG[1,2]*, STEVEN E. KOCH[3], CHRISTOPHER A. DAVIS[1] and MICHAEL L. KAPLAN[2]

[1]*National Center for Atmospheric Research*†, *USA*
[2]*North Carolina State University, USA*
[3]*National Oceanic and Atmospheric Administration, USA*

(Received 18 February 2000; revised 20 April 2001)

SUMMARY

Detailed diagnostic analyses are performed upon a mesoscale numerical simulation of a well-observed gravity-wave event that occurred on 4 January 1994 along the East Coast of the United States. The value of using wavelet analysis to investigate the evolving gravity-wave structure and of using potential vorticity (PV) inversion to study the nature of the flow imbalance in the wave generation region is demonstrated. The cross-stream Lagrangian Rossby number, the residual in the nonlinear balance equation, and the unbalanced geopotential-height field obtained from PV inversion are each evaluated for their usefulness in diagnosing the flow imbalance. All of these fields showed clear evidence of strong imbalance associated with a middle-to-upper tropospheric jet streak, and tropopause fold upstream of the large-amplitude gravity wave several hours before the wave became apparent at the surface.

Analysis indicates that a train of gravity waves was continuously generated by geostrophic adjustment in the exit region of the unbalanced upper-level jet streak as it approached the inflection axis in the height field immediately downstream of the maximum imbalance associated with the tropopause fold. A split front in the middle troposphere, characterized by the advance of the dry conveyor belt above the warm front, was overtaken by one of these propagating waves. During this merger process, a resonant interaction resulted, which promoted the rapid amplification and scale contraction of both the incipient wave (nonlinear wave development) and the split front (frontogenesis). The gravity wave and front aloft became inseparable following this merger. The situation became even more complex within a few hours as the vertical motion enhanced by this front–wave interaction acted upon a saturated, potentially unstable layer to produce elevated moist convection. An analysis of the temporal changes in the vertical profile of wave energy flux suggests that moist convective downdraughts efficiently transported the wave energy from the midlevels downward beneath the warm-front surface, where the wave became ducted. However, pure ducting was not sufficient for maintaining and amplifying the waves; rather, wave-CISK (Conditional Instability of the Second Kind) was crucial.

This complex sequence of nonlinear interactions produced a long-lived, large-amplitude gravity wave that created hazardous winter weather and disrupted society over a broad and highly populated area. Although gravity waves with similar appearance to this large-amplitude wave of depression occasionally have been seen in other strong cyclogenesis cases involving a jet streak ahead of the upper-level trough axis, it is unknown whether other such events share this same sequence of interactions.

KEYWORDS: Geostrophic adjustment Split front

1. INTRODUCTION

Uccellini and Koch (1987) showed that mesoscale gravity waves frequently appear in the vicinity of upper-level jet exit regions and on the cool side of a surface warm

* Corresponding author: Dept of Atmospheric Sciences, Texas A&M University, College Station, 77843-3150, USA. e-mail: fzhang@tamu.edu

† The National Center for Atmospheric Research is sponsored by the National Science Foundation of the United States.

or stationary front. They suggested that such waves are generated as an unbalanced jet streak advances beyond the geostrophic wind maximum at the base of the trough and toward an inflection point in a diffluent height field. Despite such evidence suggesting observed mesoscale gravity waves can be generated by geostrophic adjustment, it has never been demonstrated whether and precisely how these waves are actually generated through the adjustment process. Neither is it clear whether or how wave energy at the jet level is transported down to low levels, nor what process(es) is (are) responsible for rapid wave amplification. In fact, other mechanisms for generating such waves may be possible, such as organized mesoscale convection (Powers and Reed 1993).

Vallis (1992) argued that the geostrophic adjustment process proceeds by reducing the energy constrained by the frozen field of potential vorticity (PV). He proved that geostrophic balance is indeed the minimum energy state for a slightly reduced set of primitive equations with a small Rossby number. More generally, Gent and McWilliams (1982) and Allen (1991) suggested that nonlinear balance is the more appropriate balance condition for the primitive equations, constrained by the Ertel PV. Farge and Sadourny (1989) discussed how energy might be transported to small scales during the geostrophic adjustment process.

Bosart *et al.* (1998, hereafter B98) used conventional observations to investigate an extraordinary large-amplitude gravity-wave event occurring on 4 January 1994. They suggested that any of three mechanisms might have generated the observed gravity waves: (1) a geostrophic adjustment associated with unbalanced flow, (2) mechanical perturbation of the wave duct by strong vertical motions, and (3) shear instability. They hypothesized that wave over-reflection and wave-CISK (Conditional Instability of the Second Kind) were possible wave amplification mechanisms, and that wave ducting (Lindzen and Tung 1976) was the primary maintenance mechanism for the dominant large-amplitude gravity wave. Wave over-reflection (Jones 1968) refers to the existence of a reflection coefficient exceeding unity for a vertically propagating gravity-wave incident on a 'critical level' (where the wave horizontal wave speed is equal to the mean wind speed in the direction of wave propagation). Wave-CISK refers to the positive feedback between internal gravity waves and latent energy provided by CISK processes (Lindzen 1974). However, limited resolution of the observations in both time and space prevented B98 from being able to evaluate the validity of these three mechanisms. This problem plagues most observational studies of gravity waves, and for this reason mesoscale models are increasingly being used to understand gravity-wave dynamics.

Detailed diagnostic analyses of numerical simulations performed of the 4 January 1994 gravity-wave event are presented here. The objectives of the present study are to (i) determine the origin of the simulated gravity waves aloft before they appeared at the surface, (ii) understand the possible role of unbalanced jet/front dynamics in the forcing of these incipient waves, (iii) describe the process by which this wave energy aloft eventually perturbed the lowest atmosphere, and (iv) investigate the role that convection played in the dynamics of the wave environment and the evolving structure of the gravity waves. Sensitivity experiments made with differing configurations of model physics and terrain (discussed in section 2) are used to develop tentative hypotheses concerning the likely gravity-wave generation and maintenance mechanisms operative in this case. A presentation of the methodology for diagnosing unbalanced flow and performing wavelet analyses appears in section 3. Resulting applications of the imbalance diagnostics and wavelet analyses are presented in sections 4 and 5, respectively. The scale-interactive dynamics governing the generation, amplification and maintenance of the large-amplitude gravity wave are investigated in section 6, followed by the summary and discussion.

TABLE 1. SUMMARY OF MM5 EXPERIMENTS (SEE TEXT)

Experiment	Grid (km)	Start time (UTC)	Moisture schemes	Purposes of experiment
Control run	36/12	0000/0300	Explicit + Kuo-Anthes/Grell	Full physics control run
No-Appalachians	36/12	0000/0300	Explicit + Kuo-Anthes/Grell	Topography effect examined by reducing mountains by 90%
Fake-Dry-A	36/12	0000/0300	None/none	Latent heating/cooling effect, fake-dry from 0000 UTC
Fake-Dry-B	36/12	0000/0300	None after 0600 UTC	Latent heating/cooling effect, fake-dry from 0600 UTC
Fake-Dry-C	36/12	0000/0300	None after 0800 UTC	Latent heating/cooling effect, fake-dry from 0800 UTC
4 km run	4	0500	Explicit	Sensitivity to grid resolution, initiated from control run

Resolutions of the coarse and fine grids are shown separately by a solidus (/), i.e. 36/12 refers to 36 km coarse/12 km fine grid; likewise, initialization ('start') times of the two grids are shown separately by a solidus.

2. MODEL CONTROL AND SENSITIVITY EXPERIMENTS

The NCAR/PSU* Mesoscale Model 5 (MM5) was used in this study to simulate the gravity-wave event (Dudhia 1993; Grell *et al.* 1995). The model was run on two grid meshes with horizontal resolutions of 36 km and 12 km. For the control run, the coarse domain was initialized at 0000 UTC 4 January 1994 with an NCEP (National Centers for Environmental Prediction) global grid analysis as the first guess and re-analysed with surface and upper-air observations. The 12 km nested grid domain was spawned at 0300 UTC from the coarse-domain simulation. The Kuo–Anthes and Grell convective parametrization schemes were used for the coarse and fine grids, respectively, and the Blackadar planetary boundary-layer scheme was used for both grids. A radiative condition was used on the upper boundary. The lateral boundary conditions for the coarse domain involved a flow relaxation scheme as obtained from analysed observations. The coarse domain provided one-way interactive boundary conditions and initial conditions for the fine domain.

The model was run for 24 hours without four-dimensional dynamic assimilation or any special initialization method; in fact, a run with 12-hour pre-forecast nudging failed to improve the simulation of the gravity waves. The use of strong balance constraints for initializing models is not recommended at the mesoscale but, on the other hand, numerically generated gravity waves will contaminate the first few hours of such model integrations. A measure of this mass-momentum adjustment process is the domain-averaged second derivative of surface pressure (which is directly related to the mass divergence tendency through the continuity equation (Manobianco *et al.* 1994)). Computation of this parameter revealed that gravity-wave disturbances due to the initial imbalances had fully subsided by 2 hours into the model forecast.

The experimental design is summarized in Table 1. Several 'fake-dry' simulations were performed, in which the phase change of water substance (condensation, evaporation, etc.) was disallowed to examine the role of diabatic effects in the gravity-wave generation, amplification, and maintenance. A 'No-Appalachians' simulation was conducted to explore the role of topography in gravity-wave generation by reducing the heights of the Appalachian Mountains to 10% of their original value while keeping the terrain elsewhere unchanged. 'Fake-Dry-A' consisted of turning off the diabatic effects from the very beginning of the simulation, whereas 'Fake-Dry-B' and 'Fake-Dry-C' consisted of turning off the diabatic effects 1 hour before and 1 hour after the first

* National Center for Atmospheric Research/Penn State University.

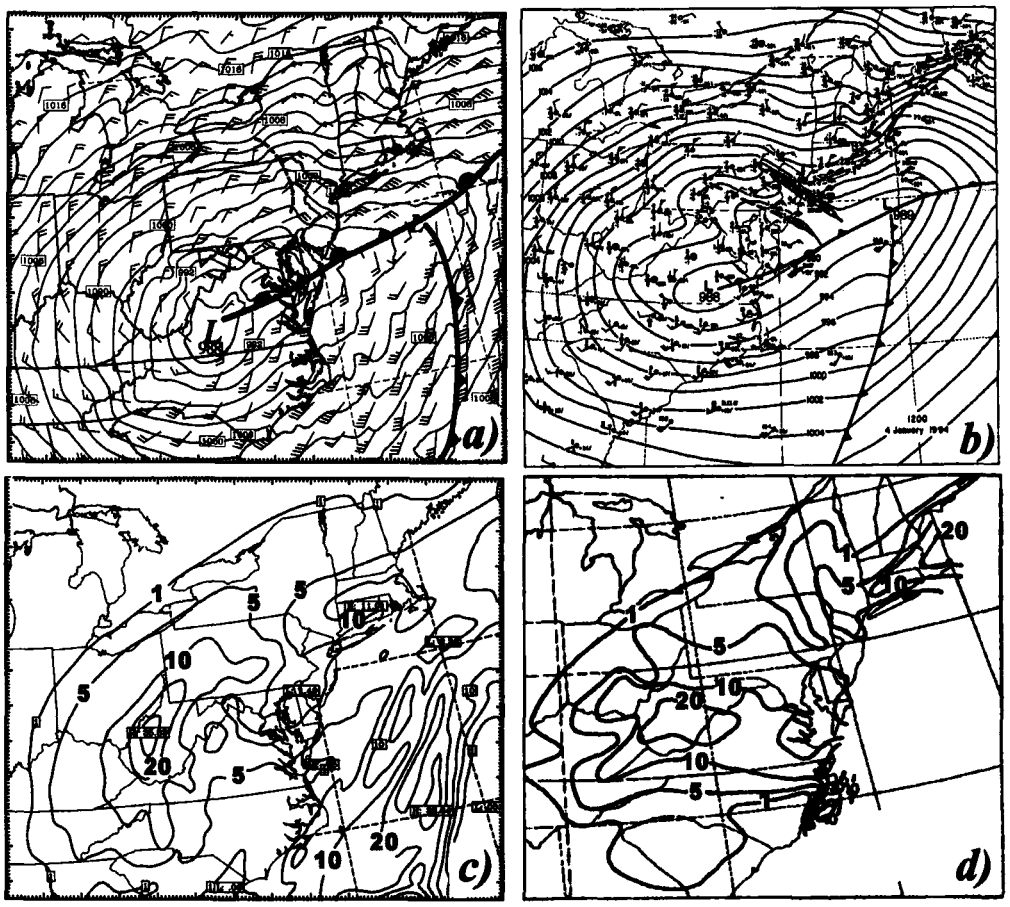

Figure 1. (a) Control run simulated sea-level pressure (every 2 hPa) and surface winds (full barb 5 m s^{-1}) for 1200 UTC 4 January 1994. (b) Subjective surface observational analysis (from Bosart *et al.* 1998). The dashed lines depict gravity-wave troughs. (c) Fine grid simulated accumulated precipitation field (solid, contoured at 1, 5, 10, 20 and 30 mm) from 0600 to 1200 UTC 4 January 1994. (d) As in panel (c) except for the observational analysis (from Bosart *et al.* 1998).

appearance of the dominant gravity wave at the surface, respectively. The '4 km run' was a simulation performed with a 4 km grid mesh initialized at 0500 UTC from the 12 km fine grid of the control simulation and with no cumulus parametrization for the innermost domain (i.e. only fully explicit microphysics was permitted). This experiment was designed to study the sensitivity of the gravity waves to the grid resolution and the uncertainties owing to the choice of cumulus parametrization scheme.

Forecast fields from the MM5 control simulation compare well with the synoptic-scale observational analysis of B98 with respect to the upper-level jet, cyclone, and surface frontal features (Figs. 1(a) and (b)). In addition, MM5 forecasted three prominent mesoscale features that were missed by the real-time models—the dominant large-amplitude gravity wave (dashed lines), a heavy snow band over the Appalachian Mountains, and a precursor warm frontal wave ahead of the cyclone. The 0600–1200 UTC accumulated precipitation field (Fig. 1(c)) shows the effect of the snow band and also a pronounced feature offshore that corresponds well with a strong convective band in the

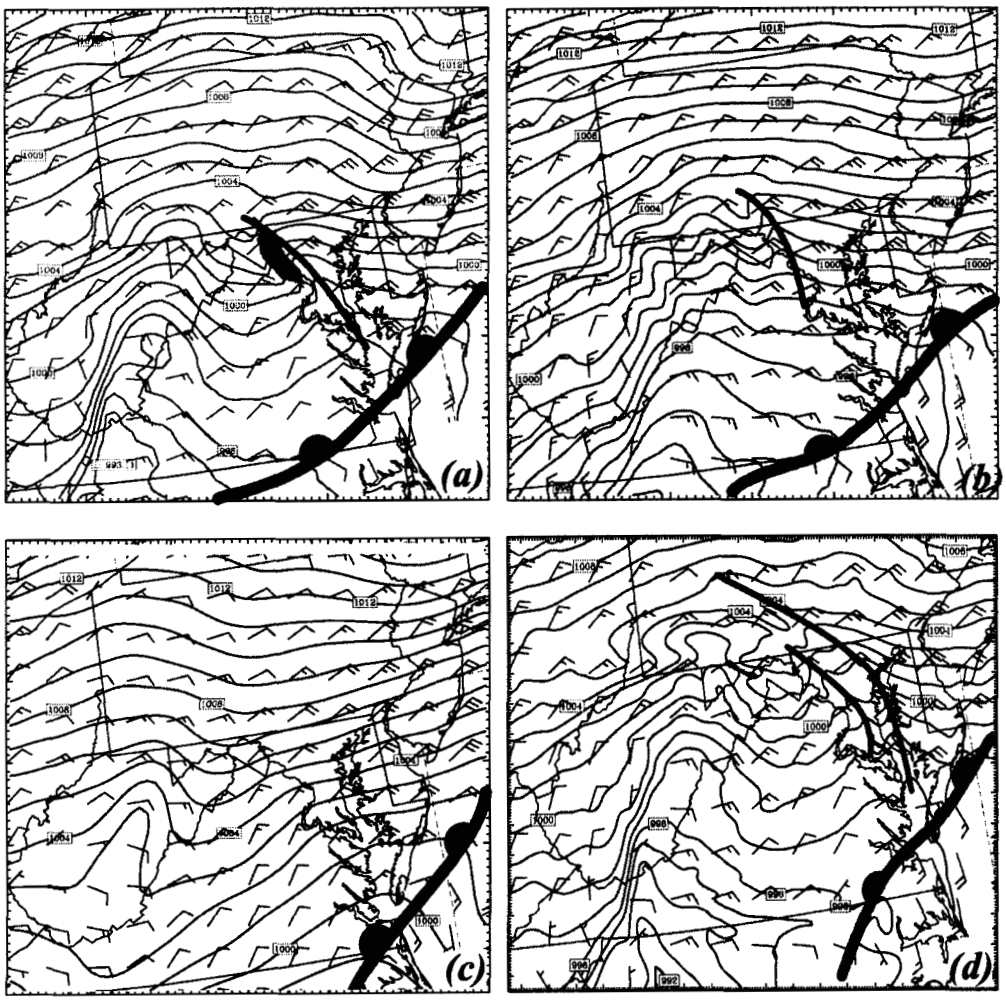

Figure 2. MM5 simulated sea-level pressure (every 1 hPa) and surface winds (full barb 5 m s^{-1}) for 0800 UTC 4 January 1994. (a) Control simulation with 850 hPa upward motion associated with the dominant gravity wave greater than 15 cm s^{-1} shaded, (b) 'No Appalachians' simulation, (c) 'Fake-Dry-A' simulation, and (d) '4 km run' simulation. Thick lines indicate the location of the dominant gravity waves. See text for further explanation.

same location seen in infrared satellite imagery (see Fig. 12 in B98), although the precipitation over extreme eastern North Carolina is underestimated (Fig. 1(d)). This rather successful precipitation forecast suggests that moist processes (including convection) were handled well in the control forecast, so that this simulation could be used to study the dynamics of the gravity wave.

The gravity wave was first detectable in the forecast mean-sea-level-pressure fields at 0700 UTC in eastern Virginia (Fig. 2(a)). This wave displayed timing, location, horizontal wavelength (~100 km) and propagation speed (22.5 m s^{-1}) similar to that observed by B98, as it propagated up the East Coast as far as eastern New York. This 'wave corridor' was similar to that observed, though perhaps ~150 km too far inland. Also, the wave fronts displayed a somewhat different orientation and shape from those analysed by B98 (Fig. 1), though there is some uncertainty in the exact wave appearance since the wave propagated quite close to the coastline. The discussion in section 4 provides

evidence that there were clear gravity-wave signals in the middle troposphere shortly before 0300 UTC in South Carolina—thus, the *actual* wave generation region was likely there, not in eastern Virginia.

The results of the sensitivity experiments suggest several testable hypotheses. When the Appalachian Mountains were removed ('No Appalachians' run), the model still produced surface frontal systems, cyclone development and gravity waves with characteristics similar to those seen in the control simulation (Fig. 2(b)). This experiment indicates that topography was not directly responsible for gravity-wave genesis. This is not altogether surprising, since the upper-level flow was south-westerly over the gravity-wave generation region, resulting in rather weak cross-mountain flow for the Appalachian Mountain range. Only weak gravity-wave activity was present aloft in the Fake-Dry-A simulation, and the dominant observed gravity wave was never realized at the surface (Fig. 2(c)). The upper-level jet and cyclone intensity also were reduced in this simulation. A slightly stronger gravity wave occurred when the latent heating was turned off one hour before the surface wave developed (Fake-Dry-B). In the simulation with the heating turned off one hour after the surface gravity wave was generated (Fake-Dry-C), the dominant gravity wave gradually weakened over the course of the next few hours (Zhang 2000). The ultra-high resolution simulation (4 km run) forecast gravity waves with characteristics similar to those seen in the control simulation (Fig. 2(d)); however, the wave spectrum expanded to include shorter waves closely associated with convection. Such grid-dependent behaviour was also seen in mesoscale model simulations of another large-amplitude gravity-wave event by Powers (1997). The results from these simulations suggest that diabatic heating played an important role in jet and cyclone development, and in the amplification and maintenance of the gravity waves, and that issues related to topography and resolution in the model could safely be ignored. This hypothesis and the roles of other processes, including geostrophic adjustment, shear instability, and wave ducting, are examined in substantial detail in the following sections.

3. METHODOLOGY

(*a*) *Unbalanced flow diagnostics*

According to the classical work by Rossby (1938), Cahn (1945), and Blumen (1972), inertia-gravity waves will be generated through geostrophic adjustment as the atmosphere tries to relieve an existing imbalance between mass and momentum. However, it has not been clearly explained what is meant by 'balanced' flow in a fully three-dimensional sense, such as with highly curved baroclinic flow. For example, in an atmosphere that obeys the quasi- or semi-geostrophic system of equations, parcel accelerations do exist, hence the mass and momentum fields are said to exist in a 'higher level of balance' with one another than if the atmosphere were purely geostrophic. Davis *et al.* (1996) point out that the underlying assumption of balanced diagnostics is that the evolution of the flow is consistent with the restrictions implicit within the diagnostic framework. There are at least five different frameworks for defining and diagnosing imbalance as reviewed extensively by Zhang *et al.* (2000). Some of these diagnostics (in isobaric coordinates) are performed in this study and summarized below. A discussion of the wavelet transform used in this study follows this exposition.

(i) *The Lagrangian Rossby number.* The first framework (and the simplest) for diagnosing flow imbalance is the Lagrangian Rossby number Ro, defined as the ratio of parcel acceleration to Coriolis force. Use of the frictionless equation of motion for the

parcel acceleration gives

$$Ro = \frac{\mathrm{d}\mathbf{V}}{\mathrm{d}t}\frac{1}{f|\mathbf{V}|} = \frac{|f\mathbf{v}_{ag} \times \mathbf{k}|}{f|\mathbf{V}|} = \frac{|\mathbf{V}_{ag}|}{|\mathbf{V}|} \approx \frac{|\mathbf{V}_{ag}|^{\perp}}{|\mathbf{V}|} \tag{1}$$

where f is the Coriolis force, $\mathbf{V}_{ag}^{\perp}$ is the ageostrophic wind perpendicular to the wind vector $\mathbf{V}$, and $\mathbf{k}$ is the unit vector. The latter approximation in this equation follows from Koch and Dorian (1988) who argued that only the ageostrophic wind normal to the flow is relevant to an assessment of flow imbalance provided that the along-stream ageostrophic wind is governed by gradient wind balance. The Rossby number in some form has been used fairly often in mesoscale gravity-wave studies to assess the existence of imbalance (Zack and Kaplan 1987; Koch and Dorian 1988; Koch and O'Handley 1997; B98; Koch *et al.* 1998).

(ii) *The residual of the nonlinear balance equation.* The nonlinear balance equation (NBE) is applicable on shorter time-scales than the quasi- and semi-geostrophic systems and is very accurate in flows with large curvature because it is quite similar to gradient wind balance (Davis and Emanuel 1991). The NBE residual is expressed as:

$$\begin{aligned} \Delta\mathrm{NBE} &= 2J(u, v) + f\zeta - \nabla^2\Phi - \beta u \\ &\cong 2J_{xy}(\partial\Psi/\partial x, \partial\Psi/\partial y) + \nabla.(f\Psi) - \nabla^2\Phi \end{aligned} \tag{2}$$

where $\beta = \partial f/\partial y$, Φ is the geopotential height, Ψ the streamfunction, and ζ the relative vorticity, respectively, while the Jacobian term $J_{xy}(u, v) = (\partial u/\partial x.\partial v/\partial y) - (\partial v/\partial x.\partial u/\partial y)$. The NBE is obtained through scale analysis of the divergence equation by dropping all terms containing the divergence, the vertical velocity, and the divergent components of horizontal velocity. Moore and Abeling (1988) discuss how in one case the nonzero sum of the terms in the NBE computed from special rawinsonde data indicated flow imbalance dominated by the divergence tendency. When the magnitude of ΔNBE is comparable with or greater than the magnitude of any individual terms on the right-hand side (r.h.s.) of (2), the nonlinear balance assumption is violated. The NBE has at times been employed with mesoscale model fields for the purpose of analysing the degree of flow imbalance. In those studies (Zack and Kaplan 1987; Koch and O'Handley 1997; Koch *et al.* 1998) a singular region of large NBE residual was found to occur within the generation region of gravity waves.

(iii) *PV inversion.* The PV inversion technique developed by Davis and Emanuel (1991) is also applied in this study. This represents the first time that PV inversion has been used to study flow imbalance for the purpose of assessing the role of the geostrophic adjustment process in the formation of gravity-inertia waves. The coupled set of equations for this technique consists of the Ertel PV (q):

$$q = \frac{g\kappa\pi}{p}\left((f + \nabla^2\Psi)\frac{\partial^2\Phi}{\partial\pi^2} - \frac{\partial^2\Psi}{\partial x\partial\pi}\frac{\partial^2\Phi}{\partial x\partial\pi} - \frac{\partial^2\Psi}{\partial y\partial\pi}\frac{\partial^2\Phi}{\partial y\partial\pi}\right), \tag{3}$$

and the nonlinear balance equation:

$$\nabla^2\Phi = \nabla.(f\nabla\Psi) + 2J_{xy}\left(\frac{\partial\Psi}{\partial x}\frac{\partial\Psi}{\partial y}\right), \tag{4}$$

where p is pressure, g is the gravitational acceleration, π is the Exner function and $\kappa = R_d/C_p$, where R_d is the gas constant for dry air and C_p is the specific heat at constant pressure.

Davis and Emanuel (1991) assumed that the irrotational part of the horizontal wind is relatively small. Under this condition, there is a unique linear (elliptic) relationship between the two unknown variables, Φ and Ψ through the NBE. Given the three-dimensional field of q from a model, the two elliptic equations (3) and (4) form a complete system, and can be solved numerically using successive over-relaxation methods. Boundary values for Φ and Ψ and their vertical derivatives on lateral boundaries are specified. The final solution turns out to be insensitive to the exact choice of boundary condition, and as long as $q > 0$ everywhere in the three-dimensional domain, a convergent solution is obtainable. 'Unbalanced geopotential' is then defined for our purposes as the deviation of Φ from that obtained using this PV inversion technique.

No single one of these methods is general enough for the study of unbalanced flow. All of the above methods can be performed upon three-dimensional mesoscale model grids. In this study, these three imbalance diagnostic tools will be employed to assess the degree of imbalance of the environment before the simulated gravity-wave generation.

(*b*) *Wavelet transform*

Wavelet transform is a relatively new data-analysis method that quite recently has been used to study atmospheric gravity waves (Sato and Yamada 1994; Grivet-Talocia and Einaudi 1998; Grivet-Talocia *et al.* 1999). An advantage of continuous wavelet transform over the traditional spectrum analysis tools like Fourier transform and spectral analysis is that it is flexible enough to provide localized time–frequency (or space–wavelength) information.

Discrete wavelet transform and continuous wavelet transform are two fundamental kinds of wavelet analysis. Continuous wavelet transform is more suitable for most real-valued geophysical time series (Weng and Lau 1994). By using continuous wavelet transform, we can project the original signal to any frequency (or wavelength) domain and thereby obtain the amplitude and phase in wave-number space. The continuous wavelet transform of a square integral function F is defined as

$$W_F(a, b) = \langle F, \mathrm{I}^*_{a,b} \rangle = a^{-1/2} \int_{-\infty}^{\infty} F(t) \mathrm{I}^* \left(\frac{t-b}{a} \right) \mathrm{d}t \tag{5}$$

where I is the base wavelet function, the asterisk denotes a complex conjugate, F is a generic function, a is the dilation parameter and b is the translation parameter (Weng and Lau 1994). Continuous wavelet transform was used to analyse the detailed three-dimensional structure and evolution of this particular gravity-wave event. The Morlet function

$$\mathrm{I}(t) = \mathrm{e}^{ik_1 t}\, \mathrm{e}^{-(|t|^2/2)}, \tag{6}$$

which is a plane wave with wave vector k_1 modulated by a Gaussian envelope of unit width, was chosen to be the base wavelet function. A practical algorithm for continuous wavelet transform using the Morlet function as the base wavelet can be found in Weng and Lau (1994), though the actual computation here was performed with the continuous wavelet-transform package accompanying MATLAB©.

4. Diagnostic analysis of flow imbalance

The 500 hPa Rossby number and NBE residual from the control simulation at 0300 and 0600 UTC estimated from the coarse grid are shown in Fig. 3. An upper-level jet streak propagated during this time from the Florida Panhandle to the South Carolina

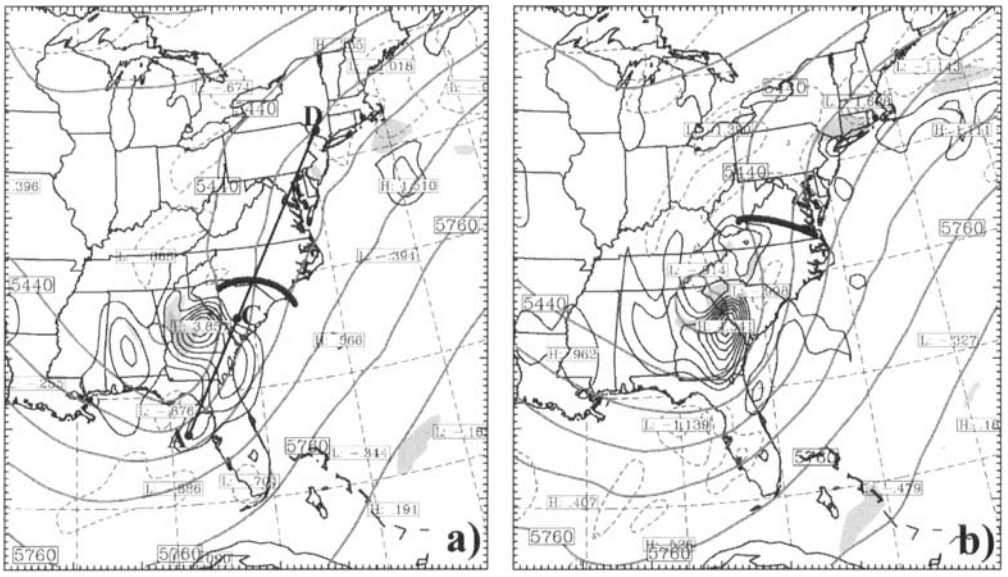

Figure 3. MM5 coarse grid simulated 500 hPa geopotential heights (thick grey lines, contour interval = 8 dam), cross-stream Lagrangian Rossby number ($Ro > 0.5$, shaded), and the residue of the nonlinear balance equation (dark full line, positive; dashed line, negative, contour interval = 0.5×10^{-8} s^{-2}) for (a) 0300, and (b) 0600 UTC 4 January 1994. Lines AD and CD depict the locations of the cross-sections shown in subsequent figures. Thick dark curves denote the location of the incipient gravity wave.

coastal region. There is clear evidence of imbalance associated with this jet streak, given the pronounced positive maximum in the NBE residual over north-eastern Georgia at 0300 UTC. This imbalance region is *directly* upstream of where the gravity wave first appeared in the model simulation. Most of the imbalance is contributed by the nonlinear Jacobian term (not shown) at the location where the zonally oriented jet streak turns rapidly poleward.

The question may be raised as to what magnitude of the NBE residual defines 'imbalance'. A complicating factor in answering this question is that the residual is highly dependent upon the model grid mesh size (Kaplan and Paine 1977). Based on scale analysis, the underlying assumption of nonlinear balance is that the magnitude of the residual of the NBE is an order of magnitude smaller than the three terms (i.e. the Jacobian, the vorticity and the Laplacian terms, respectively) on the r.h.s. of (2). The NBE residual is considered to be large (flow unbalanced) when the scale assumption of nonlinear balance is violated, that is to say when the magnitude of the NBE residual is comparable with the magnitude of any of the three terms on the r.h.s. of (2). In this case, the maximum of residual at 0300 UTC (Fig. 3(a)) is 3.8×10^{-8} s^{-2}, which is comparable with (or even larger than) the maximum of those three individual terms on the r.h.s. of (2) (not shown, but 2.7, 2.1, and 2.3×10^{-8} s^{-2}, respectively). This is also true at 0600 UTC. Thus, the flow is strongly unbalanced.

A local maximum of cross-stream Rossby number, Ro, appears approximately collocated with the maximum NBE residual in northern Georgia. The full Ro (not shown) at this location was dominated by curvature effects at the base of the trough (i.e. winds were subgeostrophic), and was of little practical utility for discerning the precise location of any imbalance. The cross-stream version of Ro advocated by Koch and Dorian (1988) was of considerably greater value in the present case, though it would appear

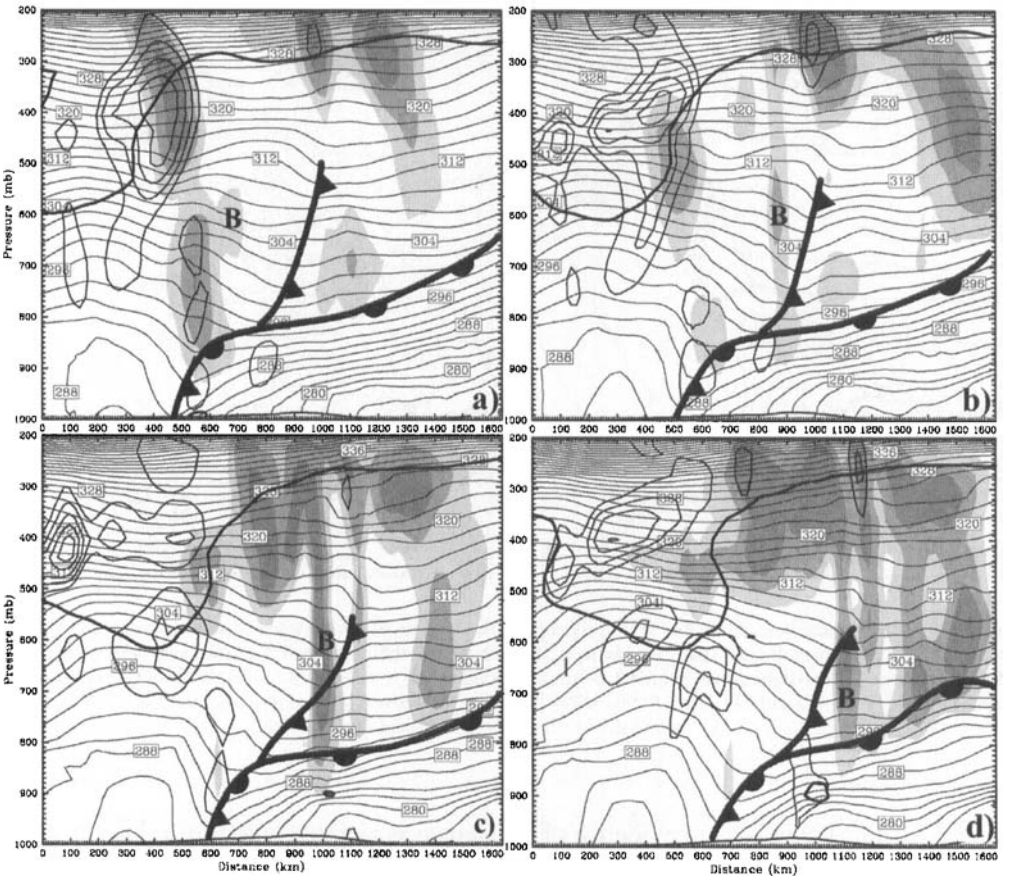

Figure 4. Cross-sections (line AD in Fig. 3(a)) of forecasted potential temperature (grey lines, contour interval = 2 K), the nonlinear balance equation residual (only $> 1.0 \times 10^{-8} s^{-2}$ are shown with dark lines, contour interval = 0.5×10^{-8} s^{-2}), and vertical velocity ($w > 3$ cm s^{-1} shaded, contour interval = 3 cm s^{-1}) valid at (a) 0200, (b) 0300, (c) 0400, and (d) 0500 UTC 4 January 1994. Thick solid lines denote the dynamic tropopause (defined by potential vorticity (PV) = 1.5 PV units). 'B' denotes the location of the incipient gravity wave.

that the residual of the NBE is a more useful imbalance indicator for the purpose of predicting gravity-wave occurrence.

Hourly analyses of the NBE residual in the cross-section plane A-D from 0200 to 0500 UTC are shown in Fig. 4. The largest residual of the NBE is found near the tropopause fold, suggesting that the imbalance was tied to the upper tropospheric front. In fact, considerable gravity-wave activity is indicated by the strong vertical motions along the dynamic tropopause at and downstream of this fold. The large-amplitude gravity wave of interest to us here first appears at 0700 UTC in the mean-sea-level pressure field ~300–500 km downstream of the strongest imbalance. No significant NBE residual appears right above where the dominant gravity wave is first seen at the surface (southern North Carolina). Rather, the *earliest* signal of the incipient wave appears in the middle troposphere at 0200 UTC as a deep band of upward motion immediately downstream of the maximum NBE residual ('B' in Fig. 4). This band rapidly amplifies and contracts in scale over the next few hours.

Geopotential heights (Φ), balanced geopotential heights (Φ_B) resulting from the PV inversion via (3) and (4), and the unbalanced heights ($\Phi_U = \Phi - \Phi_B$) computed from

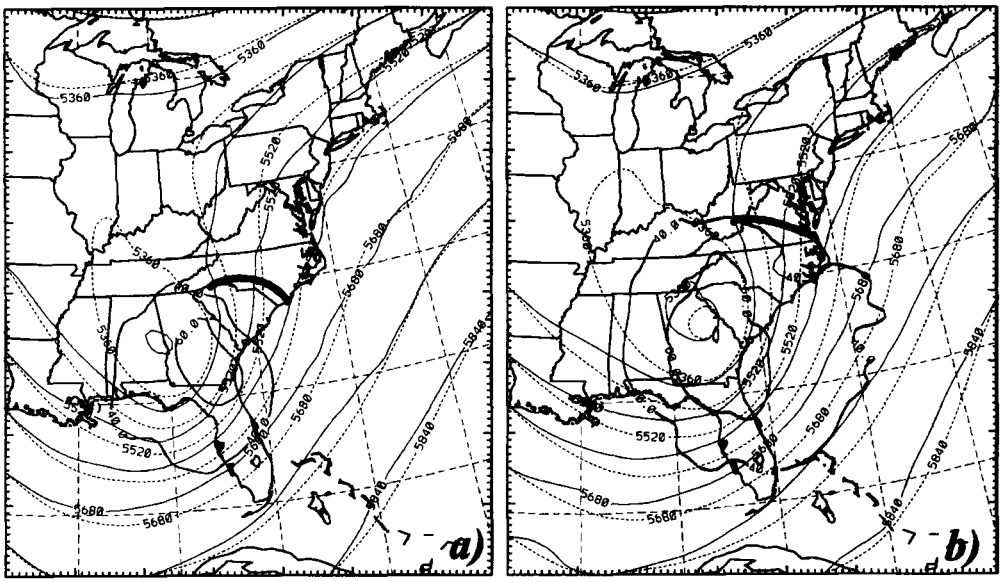

Figure 5. MM5 coarse domain simulated 500 hPa geopotential heights (full lines, dam), balanced geopotential heights from potential vorticity inversion (dashed lines, dam), and unbalanced geopotential heights (thick full lines, contour interval = 2 dam) for (a) 0300 UTC and (b) 0600 UTC 4 January 1994. Thick curve denotes the location of the incipient gravity wave.

the control simulation appear in Fig. 5. The imbalance suggested from the PV inversion is to a large extent consistent with that from the NBE analysis (Fig. 3), in that the most significant unbalanced heights ($\Phi_U > 60$ m) are over Georgia at 0300 UTC. The major gravity wave forms aloft over South Carolina on the downstream edge of this unbalanced height area. The area and magnitude of imbalance are both larger at 0600 UTC, and there is also some evidence of imbalance caused by offshore convection (this is discussed in section 6(b)(i)).

The unbalanced height from the PV inversion can be linked to the residual of the NBE by the following argument. The balanced stream function is nearly the same as the total stream function, whereas this is not true for the geopotential. Hence,

$$\Psi \approx \Psi_B;\ \Phi = \Phi_B + \Phi_U. \tag{7}$$

Since according to (2) we have,

$$2J_{xy}\left(\frac{\partial\Psi_B}{\partial x}\frac{\partial\Psi_B}{\partial y}\right) + \nabla.(f\nabla\Psi_B) - \nabla^2\Phi_B = 0, \tag{8}$$

and

$$\Delta\text{NBE} = 2J(u, v) + f\zeta - \nabla^2\Phi = 2J_{xy}\left(\frac{\partial\Psi}{\partial x}\frac{\partial\Psi}{\partial y}\right) + \nabla.(f\nabla\Psi) - \nabla^2\Phi \tag{9}$$

then we have the relationship,

$$\Delta\text{NBE} \approx 2J_{xy}\left(\frac{\partial\Psi_B}{\partial x}\frac{\partial\Psi_B}{\partial y}\right) + \nabla.(f\nabla\Psi_B) - \nabla^2(\Phi_B + \Phi_U) = -\nabla^2\Phi_U \propto \Phi'_U. \tag{10}$$

Thus, the local unbalanced positive maximum of geopotential heights tends to be correlated with the local maximum of the NBE residual.

In summary, the cross-stream *Ro*, NBE residual, and unbalanced geopotential fields show clear evidence of strong imbalance 300–500 km upstream of where the large-amplitude wave first became apparent at the surface. Geostrophic adjustment may therefore have played an important role in initiating the incipient gravity waves. In the following section, wavelet analysis will be used to track the formation and early growth of these initial waves at different scales.

5. WAVELET ANALYSIS

The vertical-motion and potential-temperature fields from the nested-grid domain simulation in a cross-section taken essentially normal to the wave fronts are displayed in Fig. 6. Upward-motion bands labelled A, B, and C represent the 200 km scale wave signals and A1, A2, B1, B2, and C1, C2 represent the 100 km scale wave signals consistent with the labelling in wavelet analysis figures to follow. During the first few hours of simulation, the vertical-motion field has a banded structure dominated by the presence of large-scale waves with wavelengths greater than 400 km. Smaller-scale wave signals begin to develop by 0300 UTC and, within the next hour, these 200 km scale wave modes already dominate the vertical-motion fields. Even smaller-scale waves A1, A2, B1, and B2 appear by 0500 UTC. The 100 km waves become a very significant mode at midlevels with the appearance of B1 and B2, which greatly modulate the existing 200 km waves. Upward-motion band B2, which grows rapidly after 0600 UTC, corresponds to the dominant gravity wave of depression that first appears in the mean-sea-level pressure field at 0700 UTC (note the downfolded isentropes below B2 near the surface).

Wavelet analyses were performed at every sigma layer, where sigma equals pressure over surface pressure, of the fine-grid model along the cross-section C-D (Fig. 3(a)) at 15 min intervals from 0300 to 0830 UTC 4 January 1994. The continuous wavelet transforms of the vertical-motion fields at 300 and 650 hPa at 0400, 0600, and 0800 UTC are displayed in Fig. 7. The abscissa in these figures represents the distance (location) in the cross-section and the ordinate represents different wavelengths. The values shown by the contours represent the wavelet density or magnitude of wavelet coefficient. Composite time–space evolutions of the 0300–0830 UTC vertical motion at 300 and 650 hPa are presented in Figs. 8(a) and (b), respectively. The corresponding wavelet coefficients at selected wavelengths of 200 and 100 km appear in Figs. 8(c) to (f).

From these various wavelet analyses we can see that gravity waves with a wavelength of ~100 km or less become pervasive at both levels by 0600 UTC, which is just before the dominant gravity wave was first seen in the sea-level pressure fields. Some of these waves are traceable back to the very beginning of the fine-grid simulation at 0300 UTC (Figs. 8(e) and (f)). However, much more apparent before 0600 UTC are incipient gravity waves with a longer wavelength (~200–300 km) at every level (though strongest around 650 hPa). The longest waves (wavelength >400 km) are most pronounced at the upper layers (300 hPa) throughout the 5.5 h period. The wavelet analysis can distinguish the growth of increasingly smaller-scale waves with time and the height dependence of the wave spectra. This downscale cascade of energy is most pronounced after 0630 UTC when convection is triggered along the crest of the 100 km wave B2 (Fig. 8(f)).

For the most part, the average wave speeds of the 200 and 100 km waves are nearly identical (~22.5 m s^{-1}) though some variation is found for the 200 km waves (Figs. 8(c) and (d)). It is particularly interesting to observe how the upward motion band over central Virginia becomes very strong at 0600 UTC just as the 200 km wave B

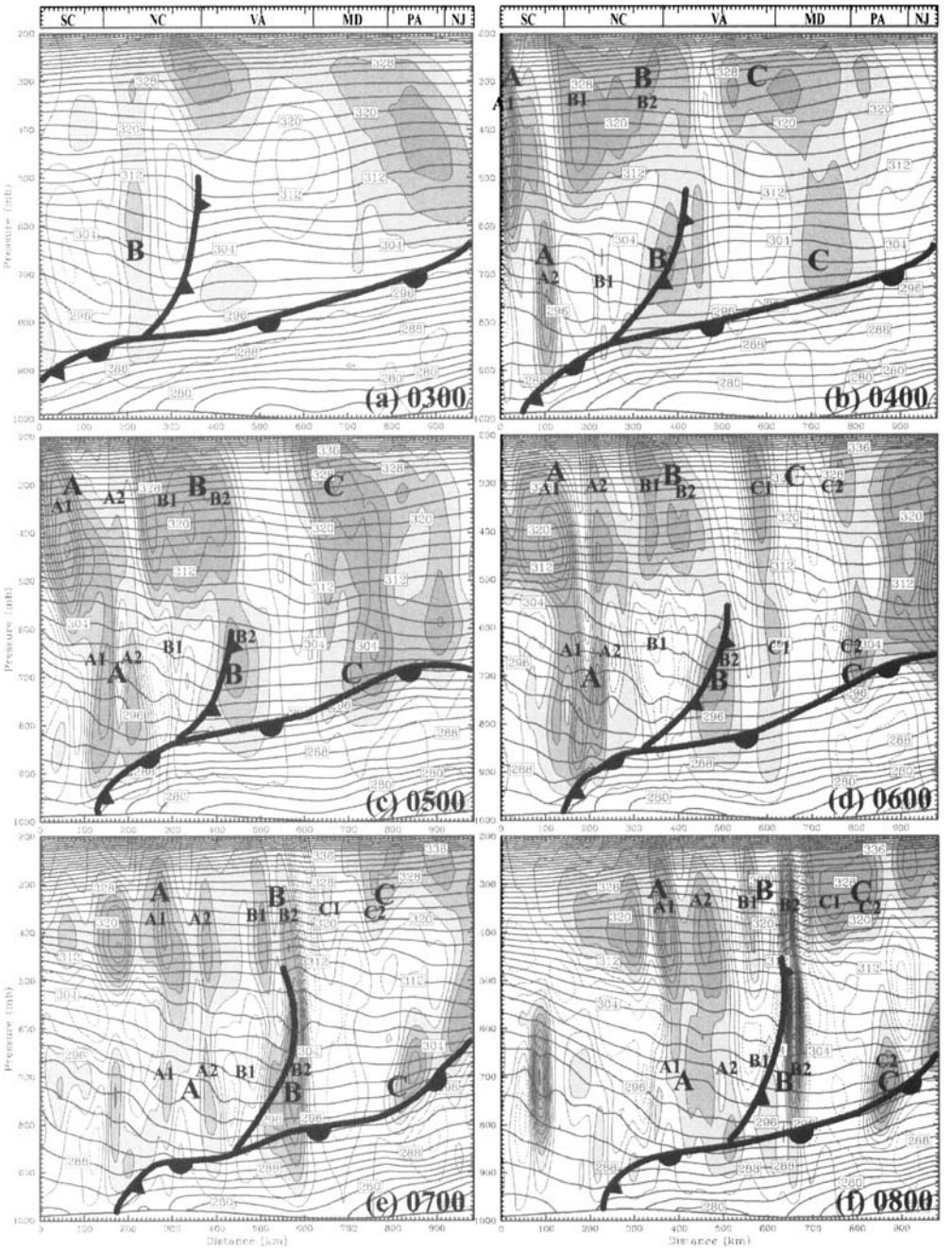

Figure 6. Vertical cross-sections alone line CD in Fig. 3(a) of forecasted potential temperature (full lines, contour interval = 2 K) and vertical velocity, w (contour interval = 3 cm s^{-1} with shaded area $w > 3$ cm s^{-1}) from the nested domain of the control simulation valid at (a) 0300, (b) 0400, (c) 0500, (d) 0600, (e) 0700, and (f) 0800 UTC 4 January 1994. Labels A, B, and C indicate the locations of the 200 km scale waves and A1, A2, B1, B2, C1, and C2 represent the locations of the 100 km scale waves as revealed by the wavelet analyses.

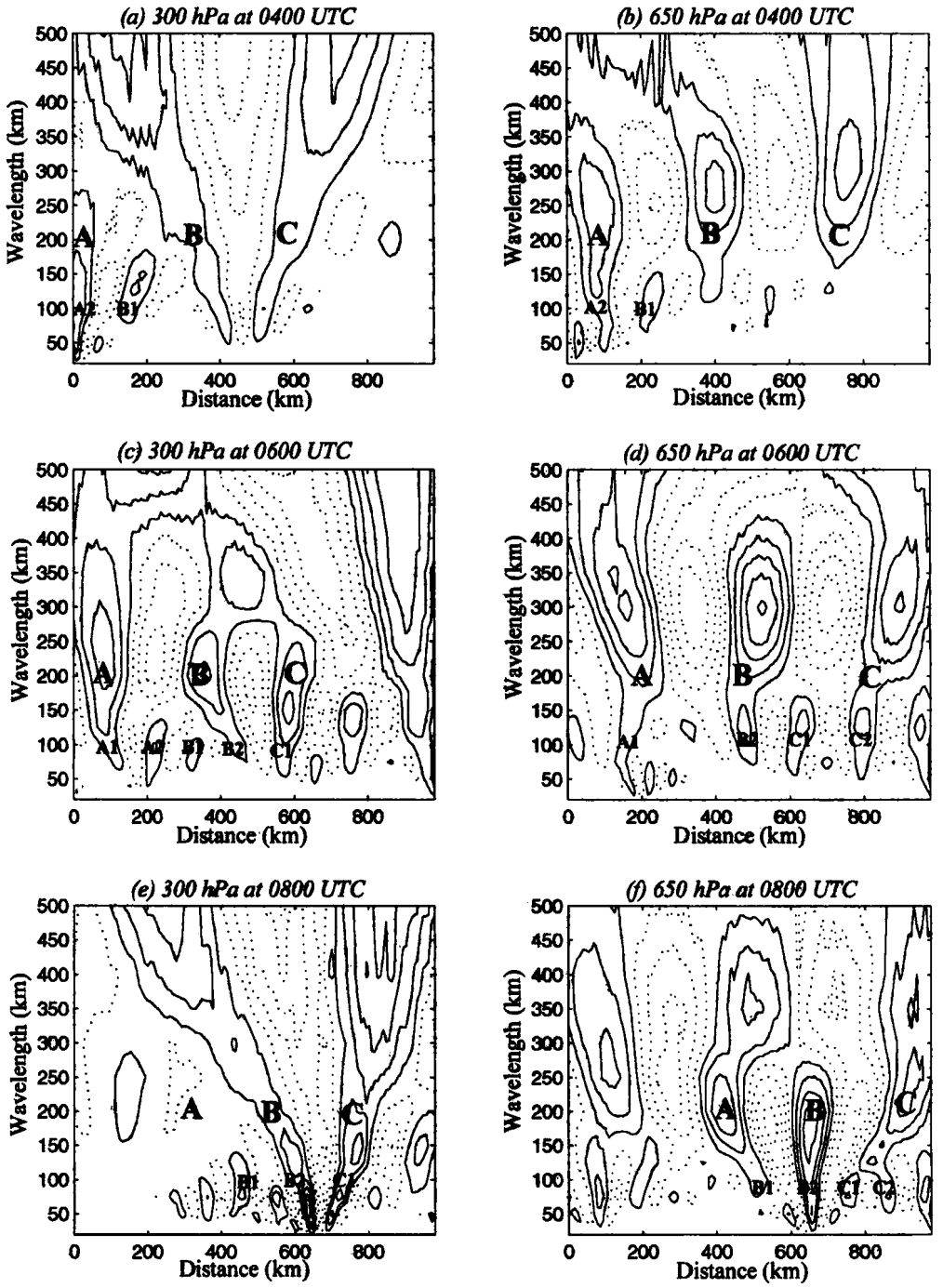

Figure 7. Continuous wavelet transform of the vertical motion along the cross-section (line CD in Fig. 3(a)) at (a) 300 hPa at 0400 UTC, (b) 650 hPa at 0400 UTC, (c) 300 hPa at 0600 UTC, (d) 650 hPa at 0600 UTC, (e) 300 hPa at 0800 UTC, and (f) 650 hPa at 0800 UTC. The X-axis represents the distance in the cross-section and the Y-axis represents different wavelengths. The value shown by the contours represents the wavelet coefficient (contour interval = 5 cm s^{-1}), with negative values shown dashed. See text for further explanation.

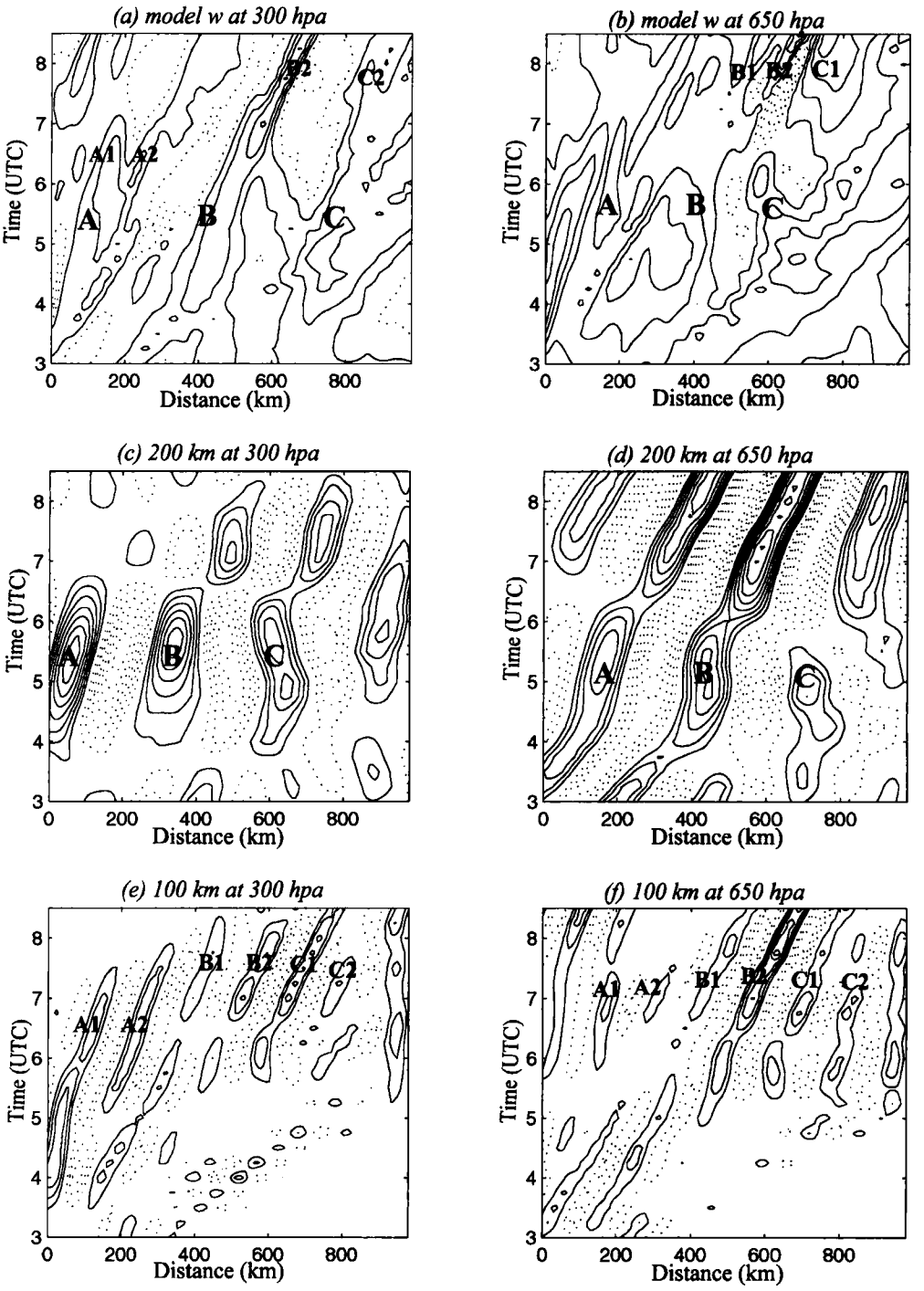

Figure 8. Time–space evolution (from 0300 to 0830 UTC) of the model vertical motion at (a) 300 hPa, and (b) 650 hPa and the wavelet coefficient at the wavelength of (c) 200 km at 300 hPa, (d) 200 km at 650 hPa, (e) 100 km at 300 hPa, and (f) 100 km at 650 hPa. Contour intervals are 5 cm s^{-1} with negative values shown dashed. See text for further explanation.

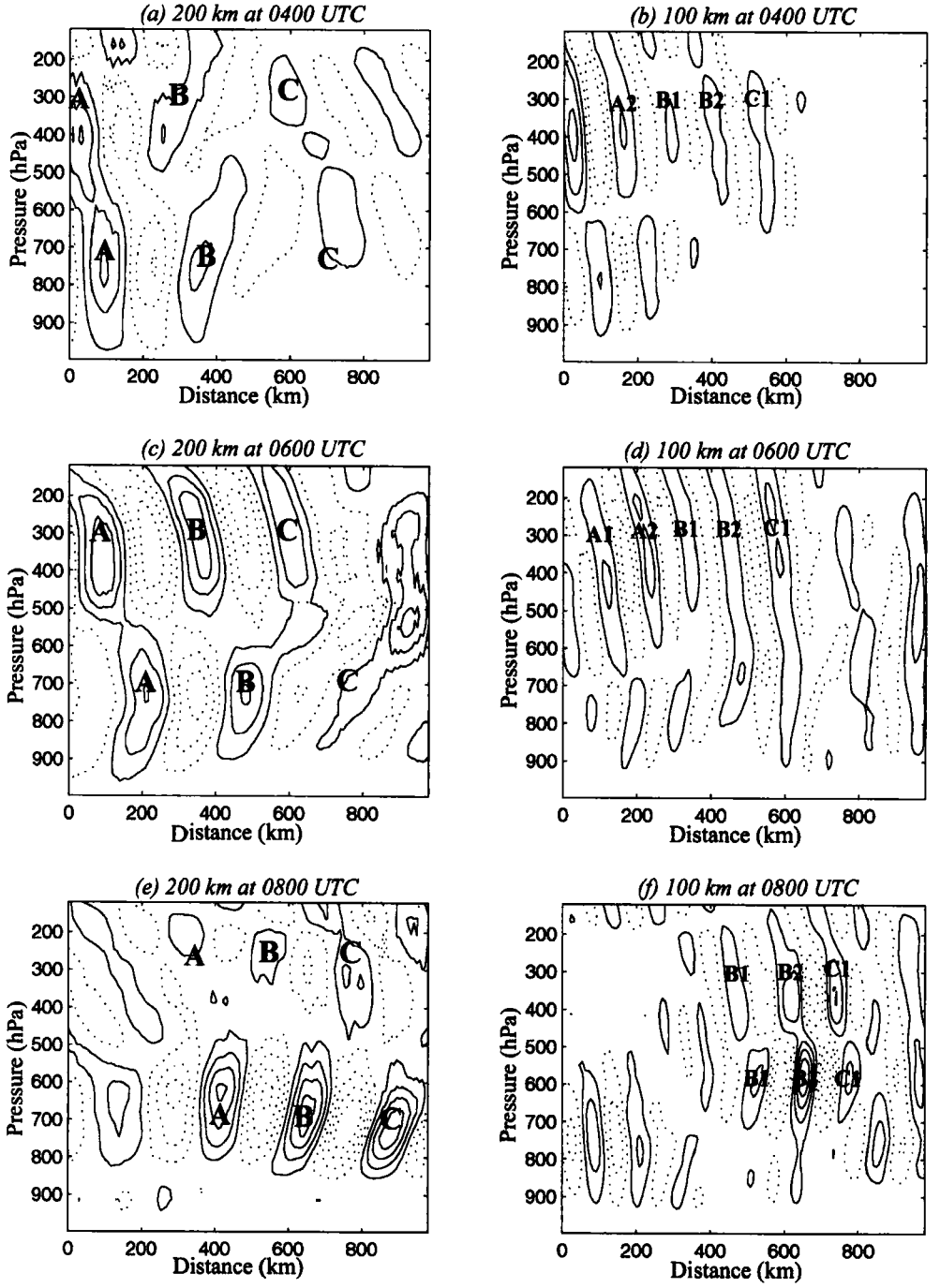

Figure 9. Vertical structure of wavelet coefficient (contour interval 5 cm s^{-1} with negative values shown dashed) at the wavelength of 200 km valid at (a) 0400, (c) 0600, and (e) 0800 UTC. (b), (d) and (f). As in panels (a), (c) and (e) except for a wavelength of 100 km. See text for further explanation.

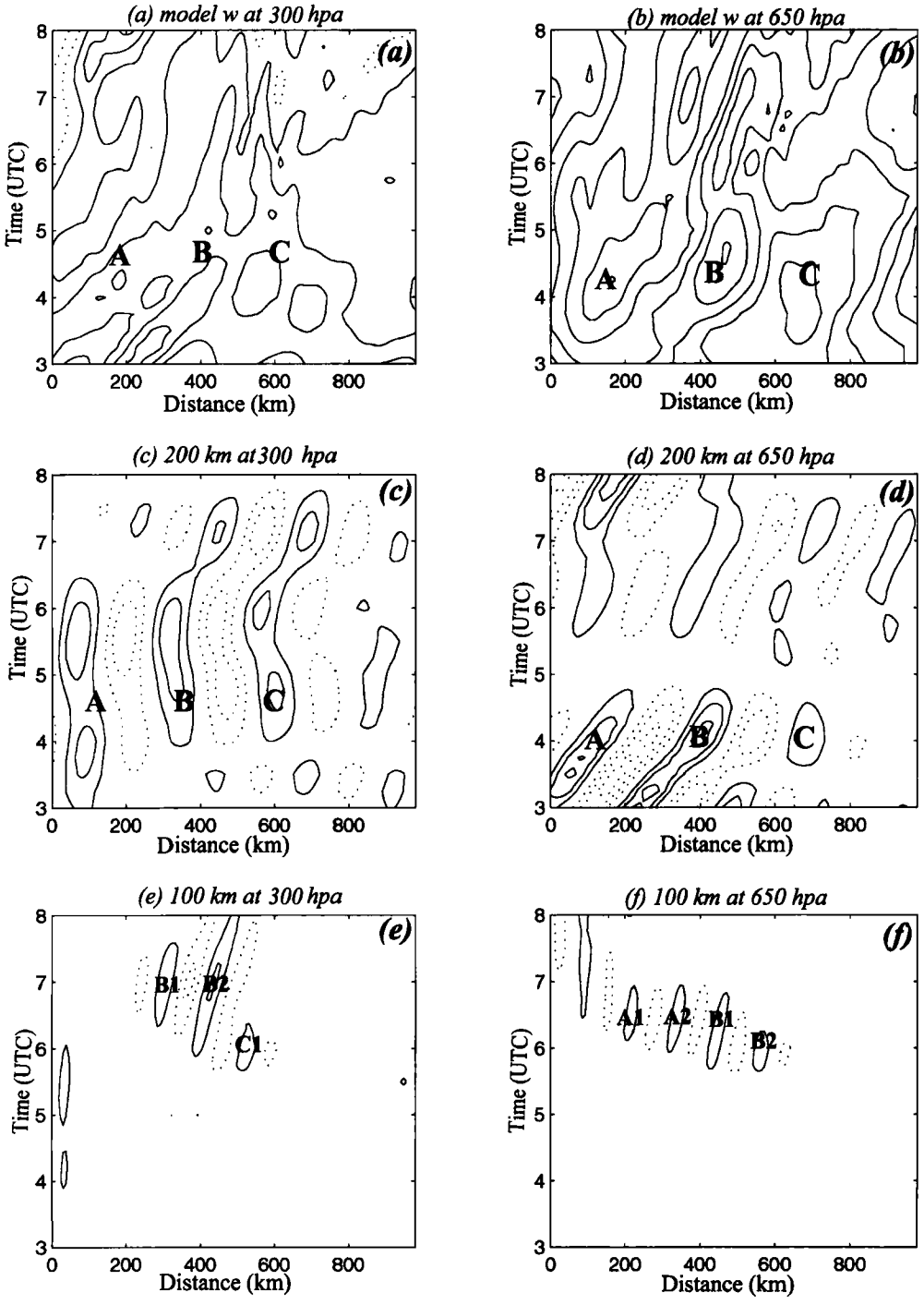

Figure 10. As in Fig. 8 except for simulation 'Fake-Dry-A'.

becomes superposed with the 100 km wave B2. However, other coherent 100 km waves did not amplify much during such temporary phasing. For example, wave A1 weakened after 0700 UTC, even though it also temporarily became superposed with wave A. Thus, nonlinear wave–wave interaction does not appear to be the mechanism by which the large-amplitude wave B2 was produced.

Detailed vertical structure of wave signals at the two representative wavelengths (100 and 200 km) is displayed in Fig. 9 at 0400, 0600, and 0800 UTC. This analysis shows that the dominant 100 km waves (B2 and C1) were first apparent in the upper-middle troposphere and displayed an upstream tilt (as did all the waves). The 200 and 100 km waves permeate the entire troposphere at 0600 UTC, thus suggesting they are fundamental wave modes during the geostrophic adjustment. The lower part of the shorter waves becomes more erect after 0700 UTC. The 200 km waves display a phase shift in the 500–600 hPa layer with maximum strength and consistency around 700 hPa. Similar results were also achieved from the wavelet analysis of other variables such as pressure, wind and temperature (not shown). Among all these variables, vertical-motion fields displayed the best signal of wave structure, origin and propagation.

Corresponding wavelet analyses of the vertical-motion fields for the Fake-Dry-A simulation are displayed in Fig. 10 for comparison with the control simulation (Fig. 8). Because the total vertical motions (Figs. 10(a) and (b)) are much weaker, the wavelet coefficients at all scales are much smaller than in the control simulation. Nevertheless, there are still signals of the incipient waves with wavelength of 200 km throughout the troposphere as early as 0300 UTC (Fig. 10(d)) and 100 km scale waves after 0600 UTC in the middle troposphere (Figs. 10(e) and (f)). Wavelet analysis performed on this fake dry simulation further indicates that the 200 and 100 km waves were both basic modes of a geostrophic adjustment process rather than the pure consequence of the model convection, whose sole influence was, in fact, to amplify the incipient gravity waves.

An experiment in which the domain size for the wavelet analysis was reduced showed no appreciable dependence of the above findings (e.g. the phase shift) on the choice of computational domain. The results from the wavelet analyses are used in combination with analyses of the wave energy transport to investigate the governing dynamics in different stages of the wave generation in the following section.

6. GOVERNING DYNAMICS OF THE GRAVITY WAVES

It has already been shown that the synoptic-scale environment associated with the upper-level jet streak was highly unbalanced shortly before the gravity waves first appeared in the middle troposphere. The governing dynamics of this evolving gravity-wave event are presented in this section in chronological order:

- Stage 1: wave generation and early development (0000–0600 UTC).
- Stage 2: wave amplification and scale contraction (0600–0800 UTC).
- Stage 3: wave maintenance (0800–1800 UTC).

The discussion of Stage 1 begins with a review of the sequence of deep adjustment processes involved in the generation of the dominant gravity wave. The presentation then proceeds to investigate the possible importance of shear instability and wave–split-front interactions in the initial development of the gravity waves. The discussion of Stage 2 emphasizes convective feedback effects on wave amplification. Wave ducting and wave-CISK processes are evaluated as possible wave maintenance mechanisms in Stage 3.

(*a*) *Stage 1: Generation and early development of the gravity waves (0000–0600* UTC*)*

(i) *Imbalance and the incipient gravity waves.* During the first 6 hours of the model simulation, the upper-level jet streak was located on the south-east side of a deep trough extending from the Central Plains to the Gulf of Mexico. The imbalance indicator fields (Figs. 3, 4, and 5) show that maximum imbalance occurred within the left exit (cyclonic shear) region of the upper-tropospheric jet, which was located at the downstream edge of the tropopause fold region. Wavelet and cross-section analyses revealed that the large-amplitude gravity wave seen later at the surface was initiated from the incipient wave band 'B' in the middle troposphere at 0200 UTC immediately downstream of the maximum NBE residual within the up-branch of the vertical circulation associated with the tropopause fold. These results imply that geostrophic adjustment associated with the upper-tropospheric jet/front system was responsible for the initiation of the incipient gravity waves. Since there was more than one wave packet and more than one wavelength, it appears that the jet dynamics could support multiple modes of nearly neutral or slowly growing waves. The process by which a single wave evolved from the initial geostrophic adjustment is addressed in section 6(a)(iii).

(ii) *Shear instability and over-reflection.* Wave over-reflection and shear instability can act as both generation and maintenance mechanisms for mesoscale gravity waves. Mastrantonio *et al.* (1976) used linear stability theory to conclude that the upper-tropospheric jet can support propagating and neutral gravity waves with wavelengths of 100–300 km. According to Einaudi *et al.* (1979), topography and convection can select the one mode that most closely matches the horizontal scale of the forcing from a large spectrum of unstable wave modes. The depth of the wave duct can also act as a modal selection mechanism. The relevance of shear instability and over-reflection to the generation of the simulated gravity waves was examined. The necessary conditions for shear instability ($Ri < 1/4$ at a critical level) were met uniquely at ~730 hPa at 0200 UTC (Fig. 11(a)). However, wave B first appeared in the 500–700 hPa layer (Fig. 4(a)), which is almost entirely above the shear instability layer. Thus, the evidence in support of the notion that wave B was generated by shear instability is not very convincing.

(iii) *Merging of the incipient wave 'B' with a mid-tropospheric split front.* Quite a bit of research has been conducted on the problem of gravity wave and internal bore generation by low-level cold fronts and density impulses. By contrast, the role of upper-level cold fronts in gravity-wave excitation has been studied very little and only quite recently (e.g. Reeder and Griffiths 1996; Griffiths and Reeder 1996; Kaplan *et al.* 1997). A major finding of the present study is that the merger of incipient wave band 'B' with a mid-tropospheric 'split front' was crucial to their mutual rapid development. According to Browning (1985), a split front has the structure of a warm occlusion as low wet-bulb potential air within the dry conveyor belt surges ahead of the surface cold front. Similar structures have been observed in the central United States, with the exception that the surface cold front is replaced by a dryline or trough, leading Hobbs *et al.* (1990, 1996) to refer to such features as a 'cold front aloft'.

Returning to the isentropic cross-sections from the coarse-mesh model (Fig. 4), it is interesting to observe that the incipient wave band B was initially located just upstream of a pronounced dip in the isentropes in the mid-troposphere, and that these isentropes

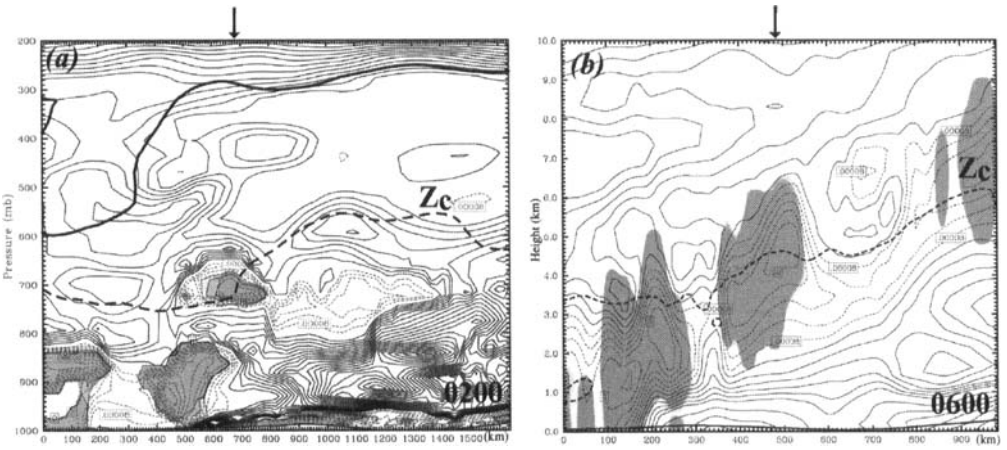

Figure 11. Cross-sections of the square of moist Brunt-Väisälä frequency (N^2, contour interval = 0.00002 s^{-2} and thin dashed lines indicate $N^2 < 0.0008$ s^{-2}). (a) Coarse grid cross-section along line AD in Fig. 3(a) in the pressure coordinate valid at 0200 UTC, and (b) fine grid cross-section along line CD in Fig. 3(a) in height coordinate valid at 0600 UTC 4 January 1994. The area shaded indicates Richardson number $Ri < 0.25$ and the thick dashed line shows the wave critical level, Zc, assuming a wave speed of 22.5 m s^{-1}. The arrows indicate the location of the gravity wave 'B' and the thick line indicates the dynamic tropopause (defined by potential vorticity (PV) = 1.5 PV units).

continually rise to the left (upstream). This structure suggests the existence of a mid-tropospheric frontal zone above the warm front. This frontal zone is more clearly identified as a split front (warm occlusion) from the equivalent potential temperature (θ_e), relative humidity, and front-relative flow fields shown in the cross-sections in Fig. 12 (which should be compared with the isentropic cross-sections in Fig. 6). The split front lies at the leading edge of increasingly pronounced horizontal gradients in θ_e and relative humidity in the mid-troposphere associated with the advancement of a dry conveyor belt.

Incipient wave B is first apparent at 0200 UTC as a slight downstream extension of the deep upward motion feature associated with the maximum NBE residual immediately downstream of the tropopause fold (Fig. 4(a)). Thus, wave B was initially 200 km behind the split front. This gravity wave propagated faster than the split front in both the coarse- and fine-grid models (Figs. 4 and 6), causing it to merge with the slower moving split front by 0500 UTC. The two regions of ascent appeared to reinforce one another as the merger took place, and by 0630 UTC this strong lifting of a saturated, potentially unstable layer (~700–600 hPa according to Fig. 12(b)) led to the development of deep, moist convection. The detailed merger process is more clearly seen in nested-grid model output at 0315, 0345, and 0415 UTC (Fig. 13). At 0315 UTC, we find a broad up-branch of the frontal circulation F ahead of the split front, with downward motion behind the front (a closed circulation system). The rising branch contracts in scale and strengthens ahead of the split front at 0345 UTC, whereas the downdraught behind the split front becomes obscured because of the approach of the incipient wave B. Complete merger occurs by 0415 UTC. Once the incipient wave B merges with the split front, they become locked in phase and inseparable.

Despite this merger, the isentropic perturbations associated with this disturbance maintain a gravity-wave behaviour. In addition, several other arguments can be offered in support of a gravity-wave interpretation. First, a simple analysis from linear wave theory shows that disturbance B is an internal gravity wave. Within the 500–700 hPa layer in which disturbance B was mainly confined before the appearance of deep

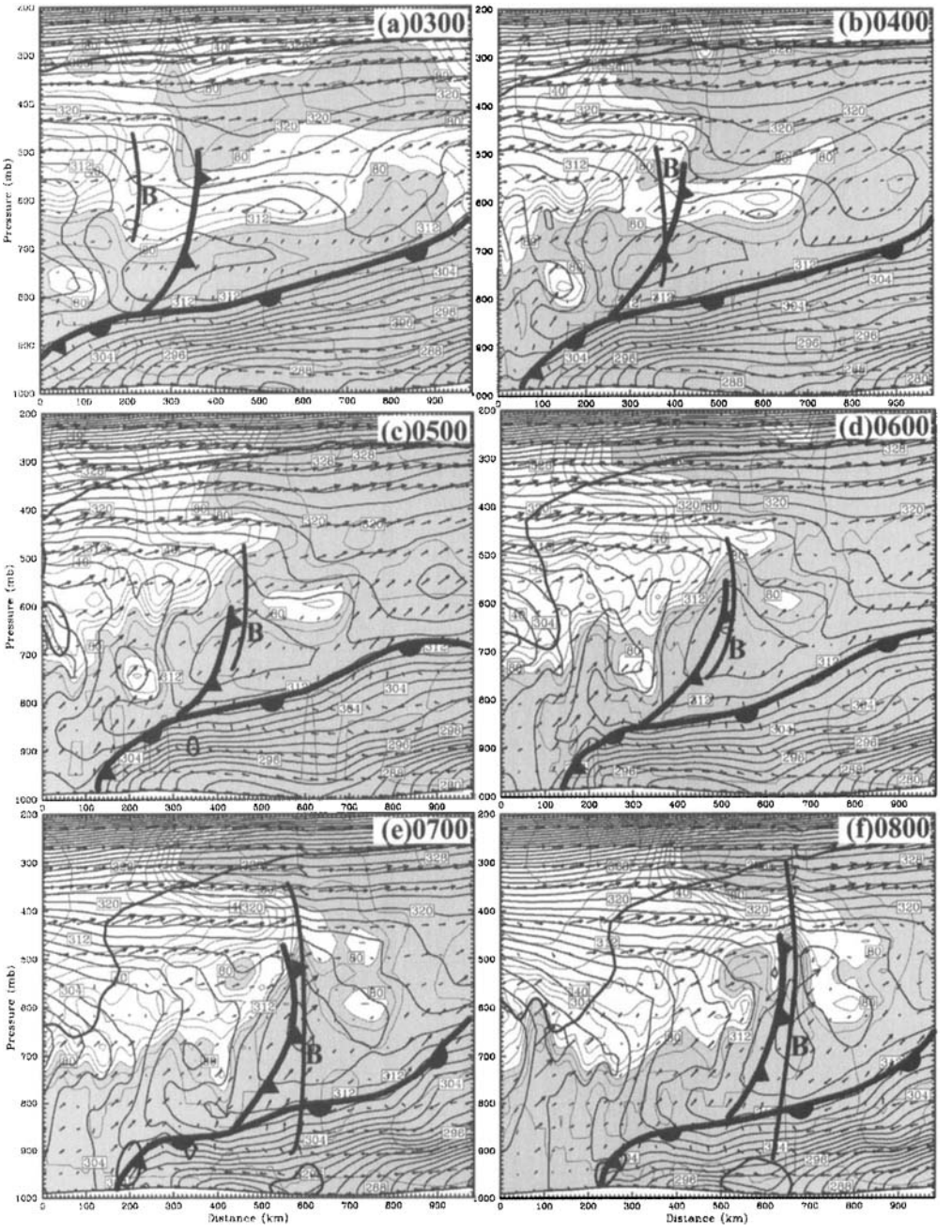

Figure 12. Vertical cross-sections along line CD in Fig. 3(a) of equivalent potential temperature (full lines, contour interval = 2 K), relative humidity (every 10% with shaded area >80%) and front-relative vertical circulation from the nested domain of the control simulation valid at (a) 0300, (b) 0400, (c) 0500, (d) 0600, (e) 0700, and (f) 0800 UTC 4 January 1994. Curve 'B' denotes the location of the gravity wave.

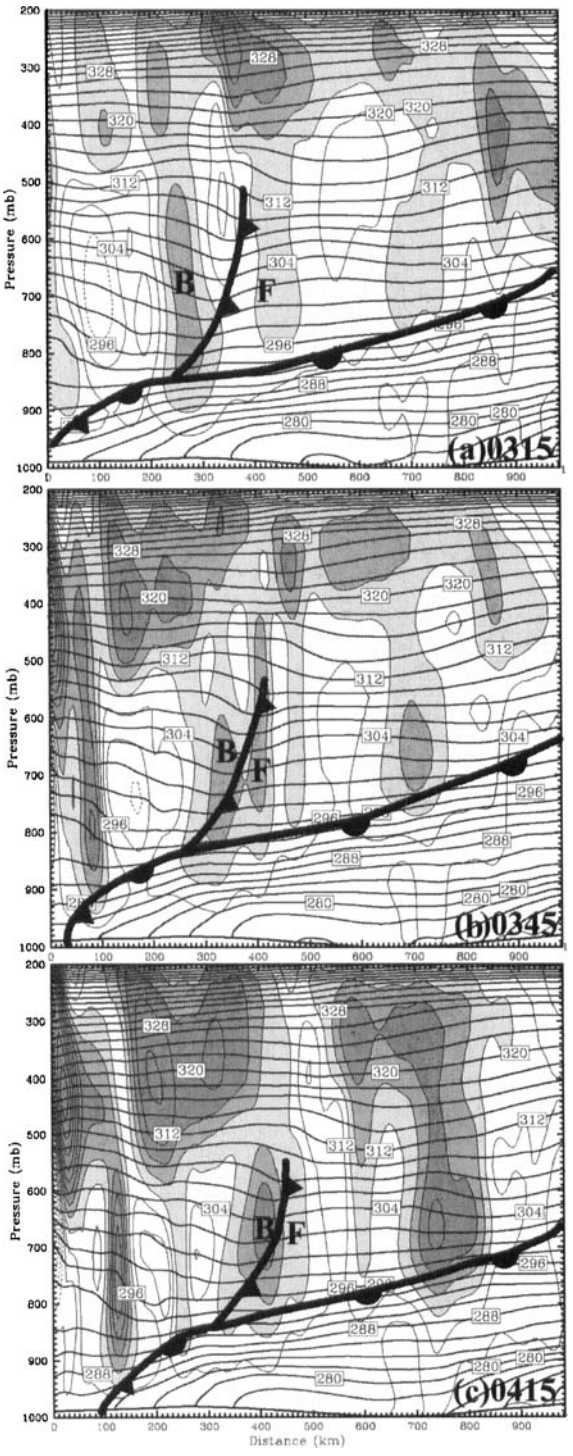

Figure 13. As in Fig. 6 except for (a) 0315, (b) 0345, and (c) 0415 UTC. 'B' denotes the location of the incipient wave and 'F' denotes the upward branch of the split-front circulation.

convection here, the moist buoyancy frequency $N \sim 0.013\ \mathrm{s}^{-1}$, and the mean wind speed in the plane of the cross-section (the wave propagation direction) $U \sim 35\ \mathrm{m\ s}^{-1}$. The half-vertical wavelength of the gravity wave is estimated from Fig. 6(e) and Fig. 9(c) as 3.8 km. Since the approximate vertical and horizontal wavelengths for disturbance B are $\lambda_z \sim 7.6$ km and $\lambda_x \sim 200$ km, the horizontal wave number (k) is much smaller than the vertical wave number (m). It follows from the wave dispersion relationship that two wave modes exist in this environment with ground-relative phase speeds of $C = U + N/m \sim 50.7\ \mathrm{m\ s}^{-1}$ and $C = U - N/m \sim 19.3\ \mathrm{m\ s}^{-1}$. Recalling that the simulated wave phase speed of disturbance B was $\sim 22.5\ \mathrm{m\ s}^{-1}$, we see that these results show that disturbance B had a phase velocity consistent with linear gravity-wave theory. Second, even after disturbance B merged with the split front and made its clear appearance at the surface, it still displayed characteristics commonly used to identify mesoscale gravity waves. In particular, the near-surface updraught centre was one-quarter of a horizontal wavelength ahead of the wave ridge (Fig. 2(a)), which is consistent with the wave polarization relation. Third, it is shown later that this disturbance travelled at a speed consistent with the ducted gravity-wave speed for the local environment. Fourth, wave B tilted upstream in a manner that is consistent with linear theory. According to the dispersion equation, the wave tilt (α) is given by

$$\tan\alpha = \left\{\left(\frac{N}{\nu}\right)^2 - 1\right\} = \left\{\left(\frac{N}{k(C-U)}\right)^2 - 1\right\} = 27.59, \tag{11}$$

where ν is the intrinsic wave frequency, the other variables have been previously defined, and the stated values for N, k, and $(C - U)$ from above have been substituted into (11). This value compares well with the wave tilt measured directly from the model simulation:

$$\frac{m}{k} = \frac{\lambda_x}{\lambda_z} = \frac{200\ \mathrm{km}}{7.6\ \mathrm{km}} = 26.32. \tag{12}$$

Rapid frontogenesis (mainly due to the tilting term) developed near the split frontal zone because of the enhanced vertical motions resulting from the merger process (not shown). The association of a gravity wave with a localized region in which frontogenesis developed rapidly brings to mind the notion from Griffiths and Reeder (1996) and Reeder and Griffiths (1996) that this region may have been highly unbalanced. However, in the present case the gravity wave clearly existed well before the time when frontogenesis along the split front exhibited symptoms of being unbalanced (i.e. after 0500 UTC). Furthermore, the gravity wave did not form within the frontal zone as required by this concept of unbalanced frontogenesis, but rather propagated into such a zone.

The hourly evolution from 0200 to 0500 UTC of θ_e, the analysed frontal systems at 600 and 1000 hPa, and the 600 hPa upward motions are shown in Fig. 14. Warm occlusion had already taken place at the surface by 0200 UTC as the coastal warm front was stalled by the persistent cold air damming to the east of the mountains in the Carolinas. The triple point was along the South Carolina coast with the cold front extending to the south and the coastal front extending to the north-east. The split front (analysed along the axis of maximum θ_e at 600 hPa) propagated north-eastward ahead of the surface occluded front and became extremely arc-shaped. The upward-motion band that identifies wave B is seen between the split front and the surface front at 0200 UTC and quickly merges with the split front by 0400 UTC. This understanding of the split-front structure also helps to explain the developing 'snow bomb' which is at the western end of the split front, while the eastern part of the split front appears to have significantly

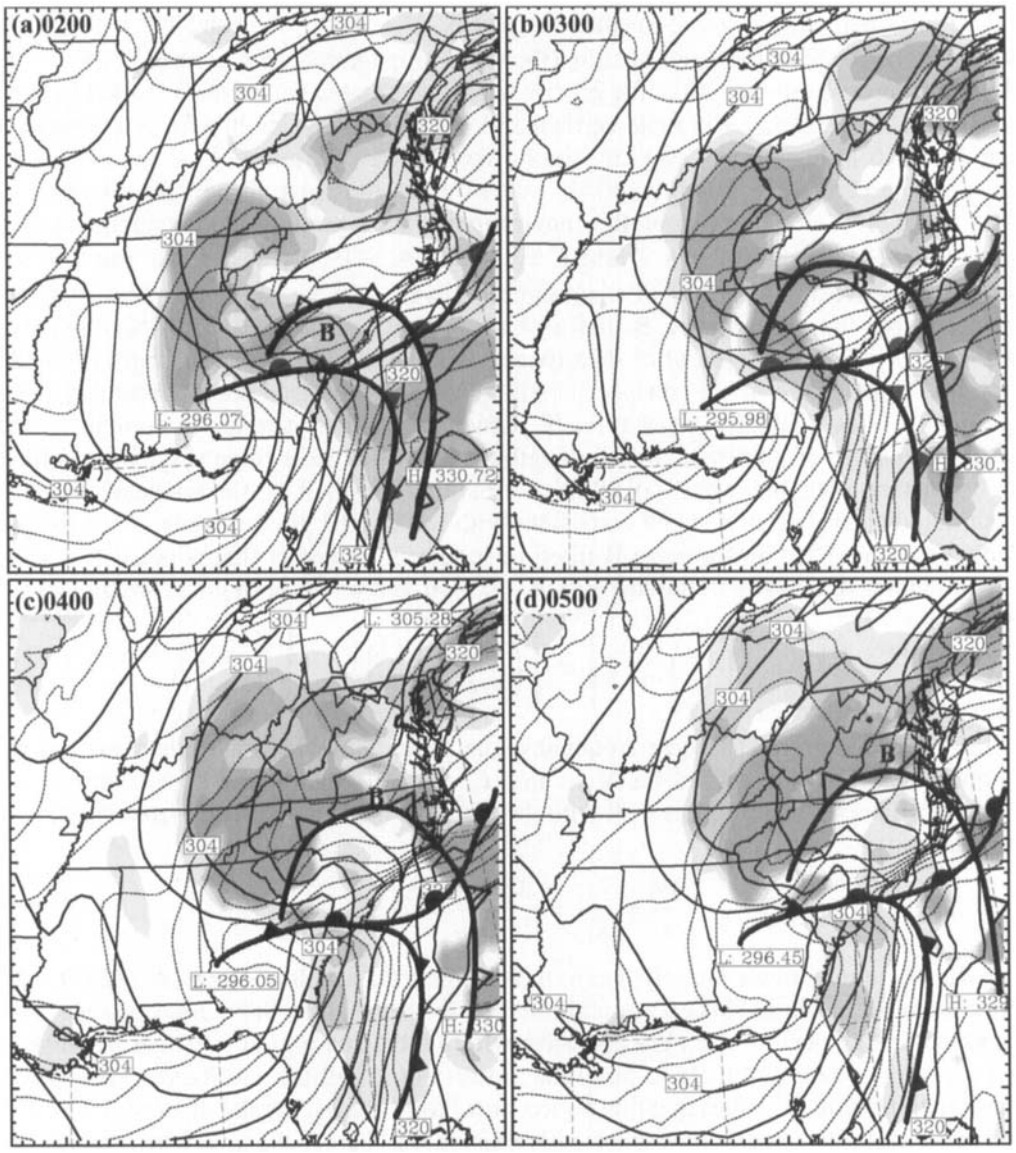

Figure 14. The coarse domain simulated equivalent potential temperature at 600 hPa (full line every 3 K) and 1000 hPa (dashed lines every 3 K) and 600 hPa upward motion (shaded every 3 cm s^{-1}) valid at (a) 0200, (b) 0300, (c) 0400, and (d) 0500 UTC 4 January 1994. Thick curves with open pips denote fronts at 600 hPa. Surface fronts are denoted in the customary fashion.

contributed to the enhancement of offshore convection. Of final mention here is that the merger of upward-motion feature B with the split front was also apparent in the fake-dry simulation (not shown).

(*b*) *Stage 2: Wave amplification and scale contraction (0600–0800* UTC*)*

It was shown above that pure shear instability was not sufficient for the rapid growth of the dominant gravity wave and the shortening of the wavelength. Although the incipient waves in the Fake-Dry-A simulation were similar to those of the control simulation (Fig. 10), without latent heating these waves never amplified, and thus never

became strong enough to be seen at the surface. Local convection triggered by the merger of wave B with the split front was the primary factor in the rapid growth of the dominant gravity wave B1, the decrease in the wavelength from 200 to ~75 km, and the appearance of the large amplitude wave of depression in the simulated mean-sea-level pressure fields.

(i) *Convective feedback effects on flow imbalance and gravity-wave dynamics.* Latent heating was very important in the *development* of the simulated gravity waves since they were noticeably absent in the fake-dry simulations (Fig. 2). However, it does not necessarily follow that gravity waves were *generated* directly by convection. A numerical model run without any latent heating is not necessarily a good test of whether large-scale geostrophic adjustment processes were the generation mechanism for the mesoscale gravity waves. The reason for this is that, as suggested by Pokrandt *et al.* (1996) and as also occurred here, in the absence of latent heating, the overall intensity of the large-scale cyclone is weakened, the wavelength between the upper-level trough and ridge becomes longer, and both parcel divergence tendency and flow imbalance are reduced. Therefore, by removing all latent heating, the synoptic-scale energetics would be substantially different from those of the actual storm, and the effects of large-scale unbalanced motions would be underestimated. Moreover, because a substantial portion of the latent heating was related to 'grid-scale' stable uplifting, those effects on the storm are also removed, and with them the ability to distinguish if the contribution from heating was due to unstable (convective) or stable motions. Mesoscale convection off the East Coast and heavy precipitation along the Appalachian Mountains contributed to the evolving flow imbalance from the very beginning of the control simulation, as proven below.

The diabatic heating from convection was estimated by several methods. First, pressure perturbation and wind-vector differences at 300 hPa at 0600 UTC obtained by directly subtracting the Fake-Dry-A simulation fields from those of the control simulation are shown in Fig. 15(a). Two regions of significant convective feedback effects are obvious—one with the snow bomb over the Appalachian Mountains and the other within the offshore mesoscale convection. Latent heating forced the geopotential height (pressure) to rise on both sides of the jet streak in its exit region (shaded regions). The rising pressure off the North Carolina coast enhanced the pressure gradient across the jet and contributed to jetogenesis and an associated strengthening of the cross-stream ageostrophic flow. Of direct relevance to the generation of flow imbalance is the fact that the air parcels became subjected to an intense mesoscale region of along-stream acceleration accompanying strong leftward-directed (cross-stream) ageostrophic flow ($\mathrm{D}\mathbf{V}/\mathrm{D}t = f\mathbf{V}_{ag} \times \mathbf{k}$) ensuing from the convection. Note also the presence of strongly convergent, cyclonic deviant flow at 700 hPa (Fig. 15(b)) directly beneath this region of strong divergent, ageostrophic deviant flow at 300 hPa (Fig. 15(a)). This low-level perturbation is a manifestation of the dramatic strengthening of the surface cyclone caused by the diabatic heating. Each term in the NBE displayed larger amplitude in the control run than the respective ones in the fake-dry run. The resulting imbalance in the control simulation forecast valid at 0600 UTC was nearly 50% stronger than in the dry simulation. Thus, this *mesoscale* convection caused the flow to be less balanced in the vicinity of where the gravity waves were generated.

The role of *local* convective latent-heat release in the dynamics of the pre-existing gravity waves was also examined. Since the latent heating/cooling due to the phase changes of water substance contributes significantly to the total diabatic heating, we first examine the vertical distribution and time evolution of these water substances.

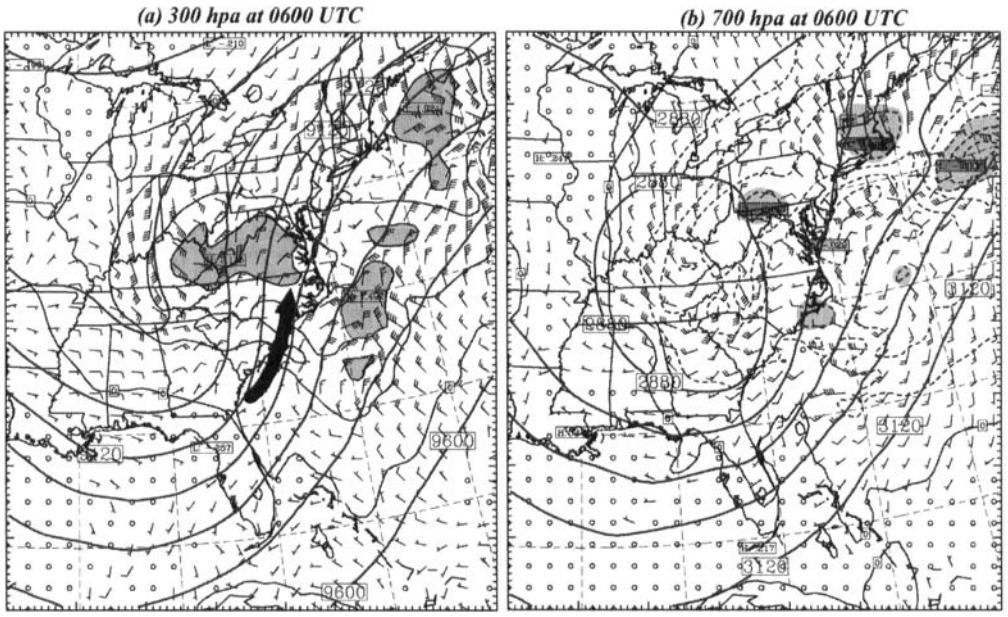

Figure 15. Difference pressure (contour interval = 1 hPa) and difference wind vector (full barb 2 m s^{-1}) between the control simulation and 'Fake-Dry-A' for (a) 300 hPa and (b) 700 hPa at 0600 UTC. Positive (negative) values (full (dashed) lines) represent larger (smaller) values in the control simulation with extrema shaded. The arrow in (a) indicates the jet location.

Vertical profiles of cloud water/ice and rain water/snow in the cross-section are displayed hourly from 0300 to 0800 UTC in Figs. 16 and 17. Scattered lower-level clouds (mostly below 800 hPa) with no attendant rain production were associated with the warm front at 0300 UTC. These clouds became more organized above the warm-frontal boundary by 0400 UTC, and began to produce precipitation streamers. The incipient gravity waves organized these clouds into three clearly separated cloud/rain bands with a spacing of ~200 km by 0500 UTC. The top of cloud band B developed rapidly upward from 800 hPa at 0300 UTC to 500 hPa by 0700 UTC. This cloud band was associated with the incipient 200 km wave B from 0300 to 0600 UTC and a combination of wave-bands B and B2 afterward (Fig. 6). This cloud band produced a distinct rain band with a horizontal dimension smaller than 100 km by 0800 UTC, with dramatic effects felt in the mean-sea-level pressure field.

The effects of the phase changes of water substance on the heating rate can be understood from the thermodynamic equation, which was solved for the diabatic heating rate as the residual of the remaining terms computed from the model grid-resolved variables:

$$\frac{\mathrm{d}\theta}{\mathrm{d}t} = \frac{\partial\theta}{\partial t} + u\frac{\partial\theta}{\partial x} + v\frac{\partial\theta}{\partial y} + \frac{\theta_0}{g}N^2 w. \tag{13}$$

Thus, the total diabatic heating rate of a parcel was estimated as the residual of the sum of the local change of the potential temperature, its horizontal advection, and the adiabatic effect due to vertical motion. The vertical distribution of the estimated diabatic heating rate in the cross-section from 0300 to 0800 UTC is shown in Fig. 18. Diabatic heating associated with the warm core of cloud band B first shows up around 700 hPa at 0400 UTC, but it is very small (~2 K h^{-1}) until 0630 UTC, when increasing cloud-water

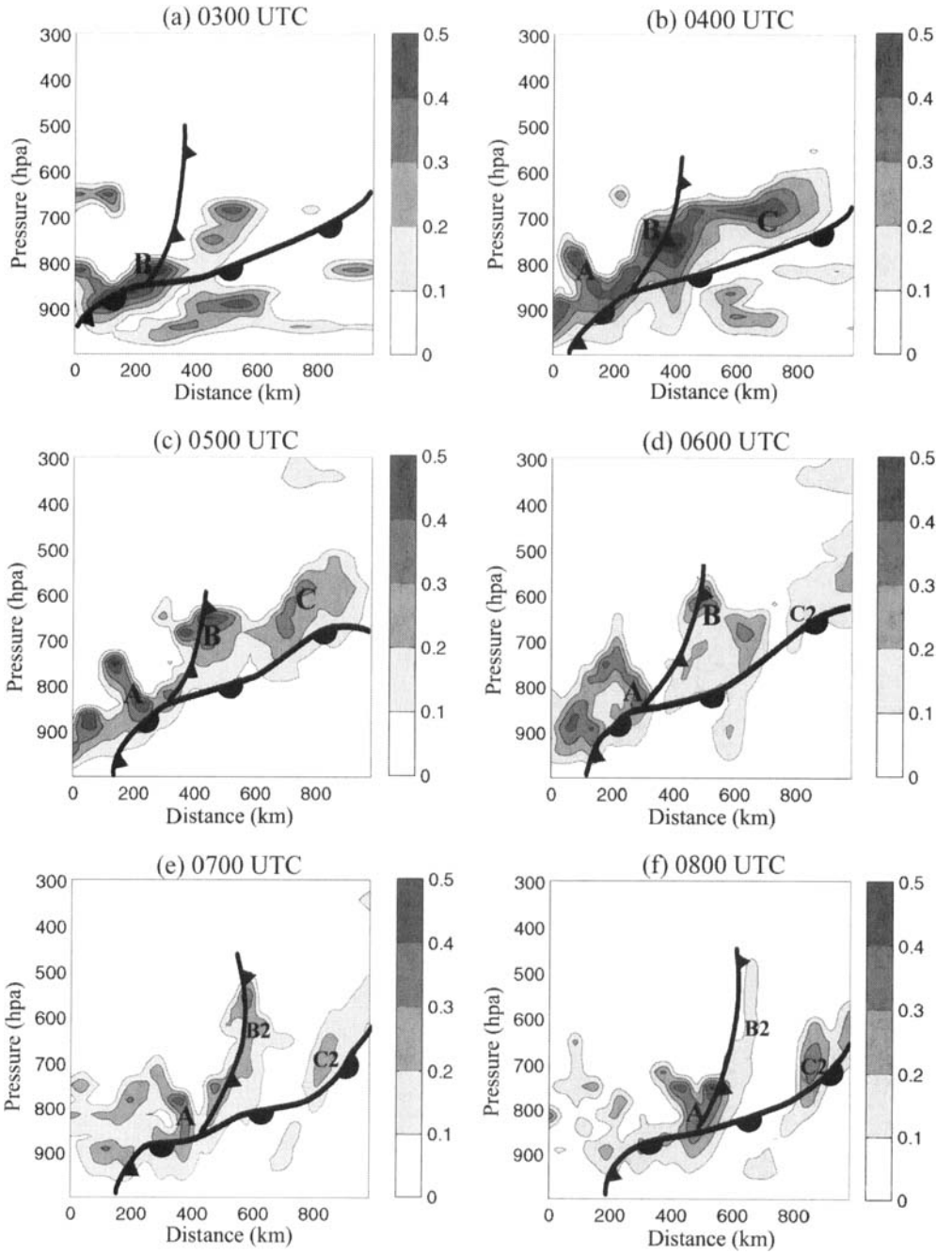

Figure 16. The vertical distribution of the cloud water/ice content (contour interval 0.1 g kg^{-1}) in the cross-section (line C–D in Fig. 3(a)) at (a) 0300, (b) 0400, (c) 0500, (d) 0600, (e) 0700 and (f) 0800 UTC. See text for further explanation.

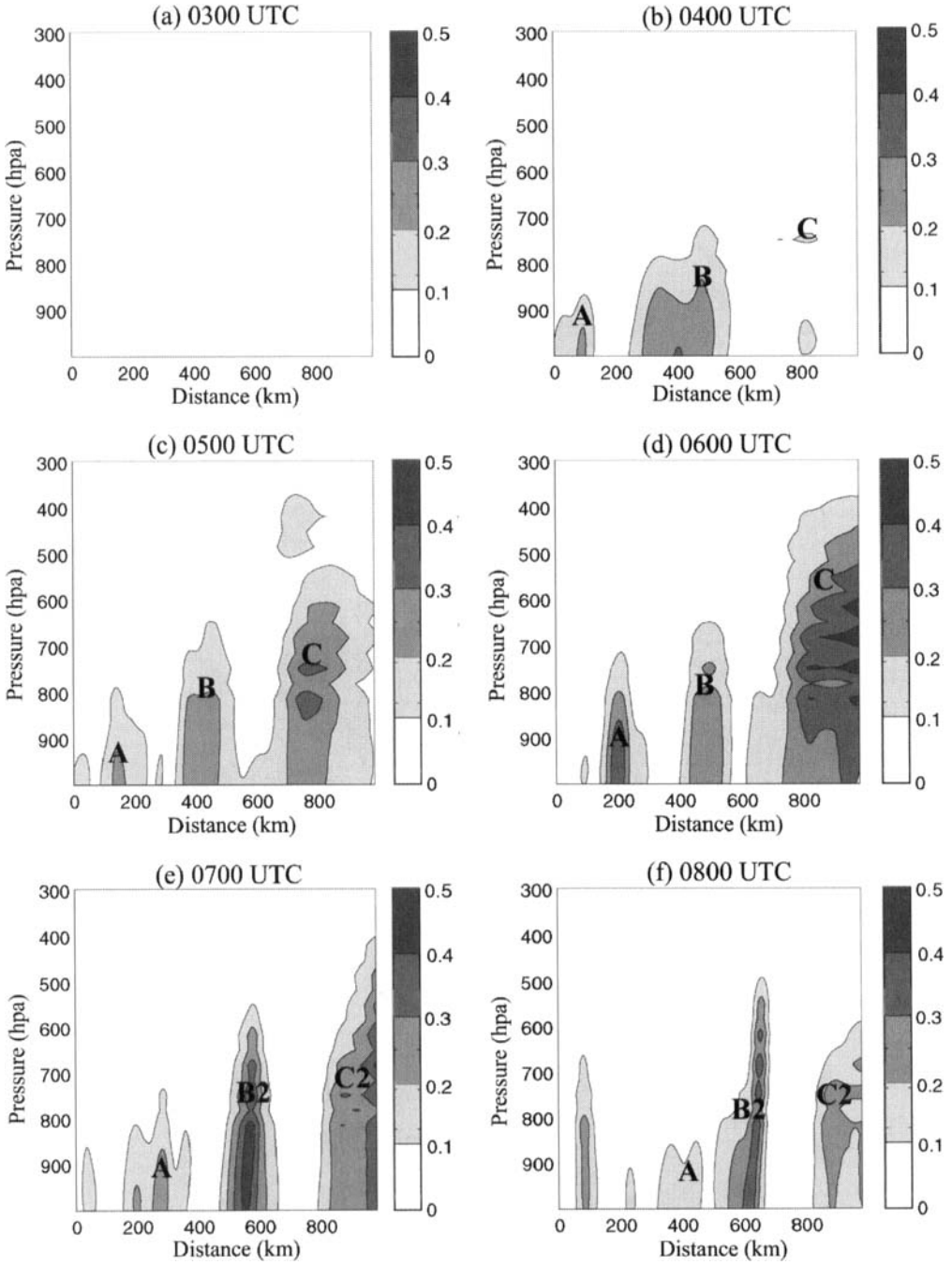

Figure 17. As in Fig. 16 but for rain water/snow.

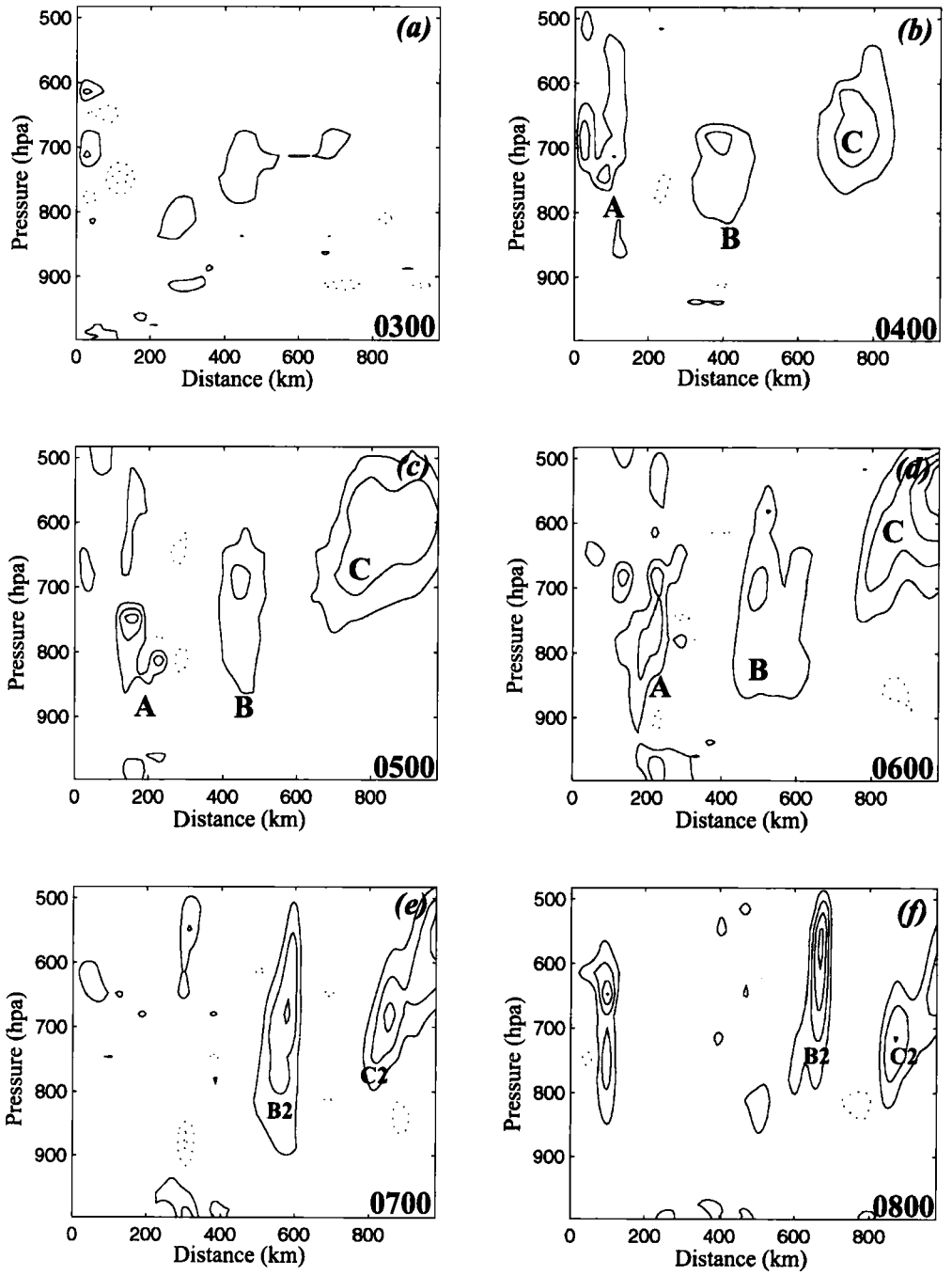

Figure 18. The vertical distribution of the hourly diabatic heating rate (contour interval 1 K h^{-1} with negative values shown dotted) along the cross-section (line C–D in Fig. 3(a)) at (a) 0300, (b) 0400, (c) 0500, (d) 0600, (e) 0700 and (f) 0800 UTC. Note that the vertical scale is different from that used in previous figures. See text for further explanation.

content above 700 hPa and rainwater production from this convective band occurs in conjunction with a dramatic increase of the heating. Simultaneous with this occurrence, gravity wave B2 (with a wavelength of ~100 km) begins to dominate over the larger-scale incipient wave B and its attendant rain band (Figs. 8(d) and (f)). In addition, the strong wave of depression begins to appear in the mean-sea-level pressure field in response to the dramatic increase of the latent heating from this convection.

In summary, large-scale convection off the East Coast of the Carolinas contributed to the enhancement of the imbalance during the geostrophic adjustment process, but it did not play a direct role in triggering the incipient waves. Rather, 'localized' convection triggered and organized by the incipient waves after 0630 UTC was essential in wave amplification.

(ii) *Energy transport.* The vertical flux of energy associated with two-dimensional plane waves is given as:

$$F_E = \frac{1}{L}\int_{-L/2}^{L/2} (p'w')\,dx, \tag{14}$$

where w' and p' represent wave perturbation quantities and the flux is averaged over one horizontal wavelength L. We chose $L = 200$ km centred around upward motion band B (Fig. 6) to estimate the fluxes throughout this study and to compute the mean background wind in the direction of wave propagation averaged over the same distance. The time-dependent profiles of energy fluxes and the mean wind in this quasi-Lagrangian framework are shown in Fig. 19.

Generally, for the incipient waves (Fig. 19(a)), there is slight downward energy transport. Although the fluxes are small around the critical level, energy flux divergence ($dF_E/dz > 0$) occurs at this level, suggesting weak energy extraction from the background flow (shear) to support further wave development. At 0600 UTC, a small amount of upward energy transport (Fig. 19(b)) becomes apparent above the strongest shear layer. Beneath the critical level (Z_c) the downward energy transport has been maintained since 0400 UTC—thus allowing for continual wave development beneath Z_c. It is likely significant that the maximum conversion of mean kinetic energy to perturbation wave energy (strongest energy flux divergence) is occurring around 600 hPa, since this is quite close to Z_c, the level of strongest gravity-wave forcing by geostrophic adjustment, and also the split-front merger zone. Finally, the energy flux profile at 0800 UTC reveals a dramatic amplification in the energy flux divergence as convection has developed by this time. Although the strongest divergence is now located above Z_c, its magnitude has tripled over that only 2 hours earlier. These results indicate that deep convection acted as the dominant gravity-wave energy source, as well as the chief means by which wave energy was transported to the lower troposphere after the incipient wave stage.

(c) *Stage 3: Wave maintenance (0800–1800 UTC)*

(i) *Wave ducting.* Geostrophic adjustment can excite gravity waves across a wide spectrum of wavelengths, and the energy can be dispersed in different directions. However, in the absence of wave maintenance mechanisms, such as wave ducting, mesoscale gravity waves may quickly lose their energy within one wave cycle and thus not be visible at the surface (Lindzen and Tung 1976; Uccellini and Koch 1987). Also, the duct properties may determine (or select) the phase speed and vertical wavelength of the dominant gravity-wave mode, hence, also the horizontal wavelength according to the wave-dispersion equation. With favourable background conditions, only certain waves

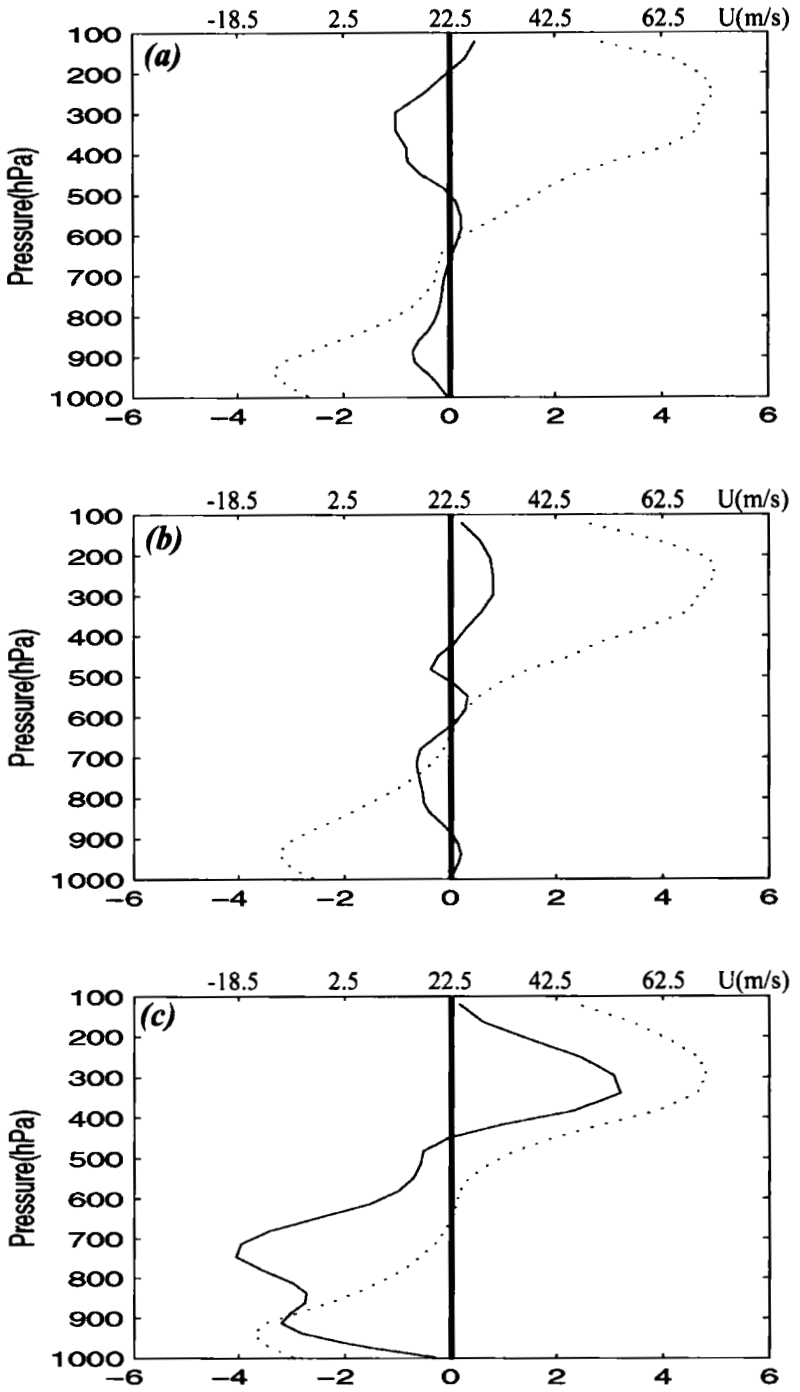

Figure 19. Vertical profile of energy fluxes (units: 0.1 kg $m^3 s^{-3}$) valid at (a) 0400, (b) 0600, and (c) 0800 UTC. The fluxes were averaged over 200 km centred around upward-motion band 'B' in Fig. 6. Dotted lines indicate the mean wind u (m s^{-1}) along the cross-section averaged over the same distance.

with specific wavelengths and speeds can be ducted, over-reflected, and thus amplified, while other waves which are not supported by this particular ducting environment will rapidly weaken.

Ducting of gravity waves was examined using the method of Lindzen and Tung (1976). The cold air beneath the warm front built up a 1.5–2.5 km thick stable layer with mean Brunt–Väisällä frequency $N = 0.012\ \mathrm{s}^{-1}$ immediately downstream of the dominant gravity wave (Fig. 11(b)). The stable-layer depth is approximately one quarter of the vertical wavelength of the gravity wave (7.6 km). A much less stable layer extending to 4–6 km overlies this duct layer. A single critical level exists in the less stable layer and $Ri < 0.25$ in a shallow region surrounding Z_c (Fig. 12). This environment provides an excellent wave duct. The intrinsic ducted wave speed is given as

$$C_{d,n} = \frac{ND}{(\pi/2 + n)}, \tag{15}$$

when n indicates different vertical wave modes and N includes the liquid-water effect. For the 'duct layer primary mode' ($n = 0$), and a duct layer of depth $D = 2.0$ km, the predicted ducted wave speed $C_d \sim 20.0\ \mathrm{m\ s}^{-1}$. Given a mean wind speed of 5 m s^{-1} in this layer, the ground relative ducted wave speed is 25.0 m s^{-1}, whereas the average simulated wave phase speed was 22.5 m s^{-1}. Thus, the necessary conditions for wave ducting according to Lindzen and Tung (1976) are satisfied for the simulated gravity waves.

(ii) *Wave-CISK.* In the absence of convective heating, the dominant gravity wave in simulation Fake-Dry-C rapidly weakened after 1000 UTC, whereas the gravity wave in the control simulation persisted for another 10 hours. Wave-CISK played a dominant role in wave maintenance. Consistent with Powers and Reed (1993) and Koch *et al.* (1998), the strongest upward motion following the generation of convection became fairly concentrated around the critical level (compare Figs. 6(d) and 11(b)). This relationship differs from the pure linear ducting theory (Lindzen and Tung 1976; Ralph *et al.* 1993). Also, the wavelet analysis showed a pronounced upstream wave tilt aloft once convection formed (Figs. 9(e) and (f)). The implication is that the wave energy source at the critical level was dependent upon convection.

This conjecture is further supported by the energy flux computations. The downward energy flux rapidly amplified, and the energy divergence at the critical level more than tripled within 2 hours after the localized convection developed (Fig. 19(c)). These structural and phase relationships are all consistent with the wave-CISK model (e.g. Raymond 1975, 1984), according to which organized convection is forced by convergence associated with a gravity wave, while latent heating within the convection provides a source of wave energy (Lin 1987). Powers and Reed (1993) termed the coexistence of wave ducting and wave-CISK a 'ducted wave-CISK mode'. This particular kind of wave structure dominates numerical simulations of gravity-wave events in the literature (Koch *et al.* 1999). Localized convection propagating with the gravity wave provides a constant source of energy and amplifies the waves, thereby compensating for the leakage of wave energy from an inefficient lower-tropospheric duct.

7. Conclusions

The MM5 numerical model simulated reasonably well a large-amplitude gravity-wave event on 4 January 1994 along the East Coast of the United States. Application of

composite wavelet analysis, wave energy transport analysis, wave ducting analysis, and various kinds of unbalanced flow diagnostics revealed a complex interaction of multi-scale processes. These interactions include those between geostrophic adjustment processes associated with an unbalanced upper-level jet, the vertical circulation transverse to a split front, latent-heat release in convection, and a train of inertia-gravity waves. Composite wavelet analysis was employed here for the first time to track unambiguously the origin, evolution, vertical structure and interactions between mesoscale gravity waves, while potential-vorticity inversion was applied here for the first time to diagnose mesoscale flow balance. A variant of the Lagrangian Rossby number and the residual in the nonlinear balance equation were also examined for their utility as imbalance diagnostic tools. Each tool showed clear evidence of increasing imbalance associated with upper-level tropopause folding immediately upstream of the large-amplitude gravity wave several hours before the first appearance of the wave at the surface.

A new conceptual model of mesoscale gravity-wave generation by geostrophic adjustment and frontal occlusion (in the form of a split front) is proposed based on our numerical simulations of this case. A schematic depiction of the generation and development of the gravity wave in association with a split front is displayed in Fig. 20. The two left panels show the initiation stage and the two right panels show the development stage in the vertical and horizontal planes. The initiation stage is characterized by the generation of the incipient gravity wave in the mid-upper troposphere immediately downstream of the maximum imbalance and the strongest up-branch of the vertical motion associated with a tropopause fold. Downstream of this incipient wave, a slower-moving split front in the middle troposphere develops a warm occlusion structure as cold, dry air within the dry conveyor belt surges ahead of and above the warm front. The merger of the incipient wave with the split front characterizes the development stage. The merger is essential to the rapid amplification and scale contraction of the incipient 200 km wavelength gravity wave. Enhanced vertical motion resulting from this merger generates a band of elevated convection within a mid-tropospheric saturated layer that is potentially unstable.

Our analysis indicated that mesoscale coastal convection enhanced the imbalance of the jet streak and cyclone evolution during the early adjustment process, but did not directly trigger the waves. In fact, incipient gravity waves also appeared in the 'fake-dry' simulations. However, by disallowing latent heating/cooling (convection) in these experiments, the waves never amplified nor appeared at the surface. After 'localized' convection was generated in the control simulation, a large amount of wave energy was transported downward to the surface through nonlinear flux-transport processes. The waves then were ducted in the low-level stable layer. Nevertheless, pure ducting was not sufficient; rather, wave-CISK was crucial for maintaining and amplifying the gravity waves because in the fake-dry simulation similar duct properties were present, yet they were not sufficient to maintain the gravity waves.

This paper has demonstrated for the first time a conceptual model for the generation of large-amplitude mesoscale gravity waves by a complex sequence of processes involving geostrophic adjustment, frontal occlusion, and convective feedback effects. This mechanism should be examined in additional gravity-wave case-studies in the future. The analysis of geostrophic adjustment processes in this study included a comprehensive evaluation of the utility of various unbalanced flow diagnostic tools for the study of mesoscale gravity waves. The relative utility of different imbalance indicators needs to be verified with more gravity-wave events and/or idealized simulations in the future. These tools should also be useful in analysing the balanced and unbalanced dynamics of many other mesoscale phenomena such as mesoscale convective systems.

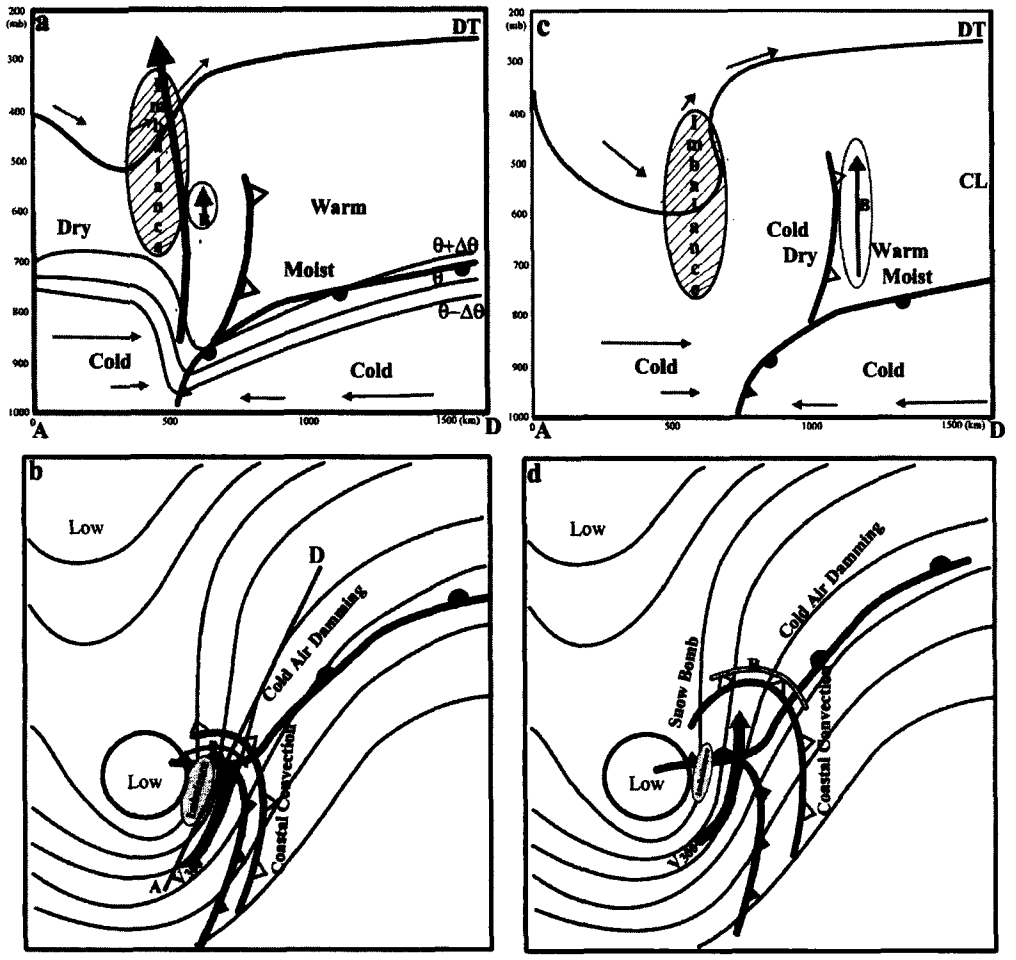

Figure 20. Schematic depiction of the gravity-wave generation by geostrophic adjustment and frontal occlusion. (a) and (b) The initiation stage: mid–upper tropospheric incipient gravity wave generated immediately downstream of the maximum imbalance when the up-branch of the tropopause fold is in phase with the surface 'occluding' front. (c) and (d) The development stage: rapid amplification of the incipient wave after it merges with a slower-moving split front which eventually triggers 'localized' convection and a large-amplitude gravity wave at the surface. Dark thick curves with solid pips denote surface fronts. Light solid curves with open pips denote split fronts at 600 hPa. Thin curves denote 300 geopotential height fields and big arrow denotes the location of the 300 hPa jet. The circled arrow in (a) and (c) and the open curve in (b) and (d) labelled 'B' indicate the locations of the incipient gravity waves.

The wavelet analysis, which was shown to be very effective for tracing the origins, vertical structure, and nonlinear interactions between the gravity waves, can also be applied as a filtering technique or scale separation tool for data assimilation, model initialization and future gravity-wave studies.

Interesting issues have been raised but not fully answered by this case-study. First, it is not clear whether the split front would have been sufficient by itself to trigger deep convection had the incipient wave not merged with it. Also, after the merger, this gravity wave became indistinguishable from the split front. This suggests that it may be difficult at times to prove that large pressure changes are caused by gravity waves. Locatelli *et al.* (1997) showed from analysis of the linear divergence equation that it may be impossible to distinguish gravity waves from split fronts on the basis of surface data

alone, because the relationships between the pressure and horizontal wind perturbations are quite similar. Finally, it is worth noting that large-amplitude waves of a depression similar to the one studied in the present case have been observed in other cases of strong cyclogenesis in which a jet streak propagated towards the axis of inflection in the upper-level height field (e.g. Bosart and Sanders 1986; Schneider 1990; Uccellini 1990; Ramamurthy *et al.* 1993). However, it is uncertain whether the precise sequence of scale-interactive processes responsible for the generation and rapid amplification of the gravity wave that has been elucidated in this study may be operative in other such events.

ACKNOWLEDGEMENTS

Discussions with Lance Bosart, Mel Shapiro, Franco Einaudi, Rich Rotunno, Chris Snyder, Jordan Powers, Mohan Ramamurthy, Yihua Wu, and Yi Jin were very helpful. The numerical computations described herein were performed on the Cray T-916 at the North Carolina Supercomputing Center, and the Cray supercomputer at the NCAR Scientific Computing Division, which also provided the initialization fields for the MM5. This research was conducted under support from a National Science Foundation grant ATM-9700626.

REFERENCES

Allen, J. S. 1991 Balance equations based on momentum equations with global invariants of potential enstrophy and energy. *J. Atmos. Sci.*, **48,** 72–76

Blumen, W. 1972 Geostrophic adjustment. *Rev. Geophys. Space Phys.*, **10,** 485–528

Bosart, L. F. and Sanders, F. 1986 Mesoscale structure in the megalopolitan snowstorm of 11–12 February 1983. Part III: A large amplitude gravity wave. *J. Atmos. Sci.*, **43,** 924–939

Bosart, L. F., Bracken, W. E. and Seimon, A. 1998 A study of cyclone mesoscale structure with emphasis on a large-amplitude inertia-gravity wave. *Mon. Weather Rev.*, **126,** 1497–1527

Browning, K. A. 1985 Conceptual models of precipitation systems. *Meteorol. Mag.*, **114,** 293–319

Cahn, A. 1945 An investigation of the free oscillations of a simple current system. *J. Meteorol.*, **2,** 113–119

Davis, C. A. and Emanuel, K. A. 1991 Potential vorticity diagnosis of cyclogenesis. *Mon. Weather Rev.*, **119,** 1929–1952

Davis, C. A., Grell, E. D. and Shapiro, M. A. 1996 The balanced dynamical nature of a rapidly intensifying oceanic cyclone. *Mon. Weather Rev.*, **124,** 3–26

Dudhia, J. 1993 A nonhydrostatic version of the Penn State–NCAR Mesoscale Model: Validation tests and simulation of an Atlantic cyclone and cold front. *Mon. Weather Rev.*, **121,** 1493–1513

Einaudi, F., Lalas, D. P. and Perona, G. E. 1979 The role of gravity waves in tropospheric processes. *Pure Appl. Geophys.*, **117,** 627–663

Farge, M. and Sadourny, R. 1989 Wave-vortex dynamics in rotating shallow water. *J. Fluid. Mech.*, **206,** 433–462

Gent, P. and McWilliams, J. C. 1982 Intermediate model solutions to the Lorenz equations: Strange attractors and other phenomena. *J. Atmos. Sci.*, **93,** 3–13

Grell, G. A., Dudhia, J. and Stauffer, D. S. 1995 'A description of the fifth-generation Penn State/NCAR mesoscale model (MM5)'. NCAR Technical Note NCAR/TN–398+STR

Griffiths, M. and Reeder, M. J. 1996 Stratospheric inertia-gravity wave generated in a numerical model of frontogenesis. I: Model solutions. *Q. J. R. Meteorol. Soc.*, **122,** 1153–1174

Grivet-Talocia, S. and Einaudi, F. 1998 Wavelet analysis of a microbarograph network. *IEEE Trans. Geosci. Remote*, **36,** 418–433

Grivet-Talocia, S., Einaudi, F., Clark, W. L., Dennett, R. D., Nastrom, G. D. and VanZandt, T. E. 1999 A 4-year climatology of pressure disturbances using a barometer network in central Illinois. *Mon. Weather Rev.*, **127,** 1613–1629

Hobbs, P. V., Locatelli, J. D. and Martin, J. E. 1990 Cold fronts aloft and the forecasting of precipitation and severe weather east of the Rocky Mountains. *Weather and Forecasting*, **5**, 613–626

1996 A new conceptual model for cyclones generated in the lee of the Rocky Mountains. *Bull. Am. Meteorol. Soc.*, **77**, 1169–1178

Jones, W. L. 1968 Reflection and stability of waves in stably stratified fluids with shear flow: A numerical study. *J. Fluid Mech.*, **34**, 609–624

Kaplan, M. L. and Paine, D. A. 1977 The observed divergence of the horizontal velocity field and pressure gradient force at the mesoscale. *Beitr. Phys. Atmos.*, **50**, 321–330

Kaplan, M. L., Koch, S. E., Lin, Y.-L. and Weglarz, R. 1997 Numerical simulations of a gravity wave event over CCOPE. Part I: The role of geostrophic adjustment in mesoscale jetlet formation. *Mon. Weather Rev.*, **125**, 1185–1211

Koch, S. E. and Dorian, P. B. 1988 A mesoscale gravity wave event observed during CCOPE. Part III: Wave environment and probable source mechanisms. *Mon Weather Rev.*, **116**, 2570–2592

Koch, S. E. and O'Handley, C. 1997 Operational forecasting and detection of mesoscale gravity waves. *Weather and Forecasting*, **12**, 253–281

Koch, S. E., Hamilton, D., Kramer, D. and Langmaid, A. 1998 Mesoscale dynamics in the Palm Sunday tornado outbreak. *Mon. Weather Rev.*, **126**, 2031–2060

Koch, S. E., Wu, Y., Jin, Y. and Zhang, F. 1999 'How predictable are mesoscale gravity waves?' Pp. 73–78 in Preprints, 8th conference on mesoscale processes. Boulder, Colorado. American Meteorological Society

Lin, Y.-L. 1987 Two-dimensional response of a stably stratified shear flow to diabatic heating. *J. Atmos. Sci.*, **44**, 1375–1393

Lindzen, R. S. 1974 Wave-CISK in the tropics. *J. Atmos. Sci.*, **31**, 156–179

Lindzen, R. S. and Tung, K. K. 1976 Banded convective activity and ducted gravity waves. *Mon. Weather Rev.*, **104**, 1602–1617

Locatelli, D. J., Stoelinga, M. T., Schwartz, R. D. and Hobbs, P. V. 1997 Surface convergence induced by cold front aloft and prefrontal surges. *Mon. Weather Rev.*, **125**, 2808–2820

Manobianco, J., Koch, S., Karyampudi, V. and Negri, A. 1994 The impact of assimilating satellite-derived precipitation rates on numerical simulations of the ERICA IOP 4 cyclone. *Mon. Weather Rev.*, **122**, 343–365

Mastrantonio, G., Einaudi, F., Fua, D. and Lalas, D. P. 1976 Generation of gravity waves by jet streams in the atmosphere. *J. Atmos. Sci.*, **33**, 1730–1738

Moore, J. T. and Abeling, W. A. 1988 A diagnostic of unbalanced flow in upper levels during the AVE-SESAME I period. *Mon. Weather Rev.*, **116**, 2425–2436

Pokrandt, P. J., Tripoli, G. J. and Houghton, D. D. 1996 Processes leading to the formation of mesoscale waves in the Midwest cyclone of 15 December 1987. *Mon. Weather Rev.*, **124**, 2726–2752

Powers, J. 1997 Numerical model simulation of a mesoscale gravity-wave event: Sensitivity tests and spectral analyses. *Mon. Weather Rev.*, **125**, 1838–1869

Powers, J. G. and Reed, R. J. 1993 Numerical model simulation of the large-amplitude mesoscale gravity-wave event of 15 December 1987 in the central United States. *Mon. Weather Rev.*, **121**, 2285–2308

Ralph, F. M., Crochet, M. and Venkateswaran, S. V. 1993 Observations of a mesoscale ducted gravity wave. *J. Atmos. Sci.*, **50**, 3277–3291

Ramamurthy, M. K., Rauber, R. M., Collins, B. P. and Malhotra, N. K. 1993 A comparative study of large-amplitude gravity wave events. *Mon. Weather Rev.*, **121**, 2951–2974

Raymond, D. J. 1975 Wave-CISK and convective mesosystems. *J. Atmos. Sci.*, **33**, 2392–2398

1984 A wave-CISK model of squall lines. *J. Atmos. Sci.*, **41**, 1946–1958

Reeder, M. J. and Griffiths, M. 1996 Stratospheric inertia-gravity wave generated in a numerical model of frontogenesis. II: Wave sources, generation mechanisms and momentum fluxes. *Q. J. R. Meteorol. Soc.*, **122**, 1175–1195

Rossby, C. G. 1938 On the mutual adjustment of pressure and velocity distributions in certain simple current systems. II. *J. Marine Res.*, **7**, 239–263

Sato, K. and Yamada, M. 1994 Vertical structure of atmospheric gravity waves revealed by the wavelet analysis. *J. Geophys. Res.*, **99**, 20623–20631

Schneider, R. S. 1990 Large-amplitude mesoscale wave disturbances within the intense Midwest extratropical cyclone of 15 December 1987. *Weather and Forecasting*, **5**, 533–558

Uccellini, L. W.	1990	'Processes contributing to the rapid development of extratropical cyclones'. Palmen memorial symposium on extratropical cyclones. American Meteorological Society, Boston, USA
Uccellini, L. W. and Koch, S. E.	1987	The synoptic setting and possible source mechanisms for mesoscale gravity wave events. *Mon. Weather Rev.*, **115**, 721–729
Vallis, G. K.	1992	Mechanisms and parameterizations of geostrophic adjustment and a variational approach to balanced flow. *J. Atmos. Sci.*, **49**, 1144–1160
Weng, H. and Lau, K.-M.	1994	Wavelets, period doubling, and time-frequency localization with application to organization of convection over the tropical western Pacific. *J. Atmos. Sci.*, **51**, 2523–2541
Zack, J. W. and Kaplan, M. L.	1987	Numerical simulations of the subsynoptic features associated with the AVE-SESAME I case. Part I: The pre-convective environment. *Mon. Weather Rev.*, **115**, 2367–2394
Zhang, F.	2000	'The role of unbalanced dynamics and topography in the generation of mesoscale gravity waves'. Ph.D. Dissertation. North Carolina State University
Zhang, F., Koch, S. E., Davis, C. A. and Kaplan, M. L.	2000	A survey of unbalanced flow diagnostics and their application. *Adv. Atmos. Sci.*, **17**, 205–218